

**NASA TECHNICAL
MEMORANDUM**

NASA TM X-64528

1970

*N71-29095 to
N71-29102*

NASA TM X-64528

STRUCTURES RESEARCH AT MSFC

**RESEARCH ACHIEVEMENTS REVIEW
VOLUME IV REPORT NO. 1**

SCIENCE AND ENGINEERING DIRECTORATE
GEORGE C. MARSHALL SPACE FLIGHT CENTER
MARSHALL SPACE FLIGHT CENTER, ALABAMA

| | | |
|-------------------|-------------------------------|------------------|
| FACILITY FORM 602 | <u>N71-29095</u> | <u>N71-29102</u> |
| | (ACCESSION NUMBER) | (THRU) |
| | <u>59</u> | <u>63</u> |
| | (PAGES) | (CODE) |
| | <u>NASA TM-X-64528</u> | <u>32</u> |
| | (NASA CR OR TMX OR AD NUMBER) | (CATEGORY) |

| | | | |
|--|---|---|--------------------------|
| 1. Report No. NASA TM X-64528 | 2. Government Accession No. | 3. Recipient's Catalog No. | |
| 4. Title and Subtitle RESEARCH ACHIEVEMENTS REVIEW, VOL. IV, REPORT NO. 1 Structures Research at MSFC | | 5. Report Date November 1970 | |
| | | 6. Performing Organization Code | |
| 7. Author(s) Jerrell M. Thomas, John R. Admire, H. J. Bandgren, R. L. McComas, W. B. Holland, B. E. Erwin, and H. M. Lee | | 8. Performing Organization Report No. | |
| 9. Performing Organization Name and Address George C. Marshall Space Flight Center Marshall Space Flight Center, Alabama 35812 | | 10. Work Unit No. | |
| | | 11. Contract or Grant No. | |
| 12. Sponsoring Agency Name and Address National Aeronautics and Space Administration Washington, D. C. 20546 | | 13. Type of Report and Period Covered Technical Memorandum | |
| | | 14. Sponsoring Agency Code | |
| 15. Supplementary Notes | | | |
| 16. Abstract 1. Saturn V test data are used in determining safety factor requirements for untested structures. Statistical data are presented that seem to yield a rational guide for choosing safety factors for untested structures. 2. A method of modal analysis of structures is presented based on repeated applications of the Rayleigh-Ritz technique using improved coordinate vectors for each iteration. Numerical examples are used to demonstrate the rapid convergence of the method. 3. A semiempirical method of estimating the flow-induced dynamic stresses in a bellows for a given set of flow conditions is formulated. Design methods for eliminating or minimizing these vibrational stresses have been developed. 4. A general purpose digital computer program is formulated for the analysis of large complex structures. The framework used in NASTRAN can be disassociated from elastic structures and applied to other disciplines. 5. Salient features of the mathematical formulation and digital algorithm developed for the Skylab docking response analysis are presented. The Apollo probe/drogue docking system is considered. 6. A payload-enclosure noise reduction study is conducted. Noise reduction of 8 to 10 dB is effected for a cylindrical structure with an internal helium environment. 7. Using a shortened S-II stage, an investigation is conducted on the longitudinal oscillation problem encountered during second stage burn of the Saturn V vehicle. Data from this test were used as direct input in developing the math model. Comparisons between flight and calculated data are made to verify the adequacy of the structural model. | | | |
| 17. Key Words (Suggested by Author(s)) Statistical determination Noise reduction Rayleigh-Ritz technique POGO Metal bellows NASTRAN Skylab | | 18. Distribution Statement Unclassified - unlimited See Document Release Form | |
| 19. Security Classif. (of this report) U | 20. Security Classif. (of this page) U | 21. No. of Pages 58 | 22. Price* \$3.00 |

PREFACE

The Research Achievements Reviews document research accomplished by the laboratories of Marshall Space Flight Center. Each review covers one or two fields of research and attempts to present the results in a form readily useable by specialists, system engineers, and program managers.

Reviews of this fourth series are designated Volume IV and will span the period from May 1970 through May 1972.

In accordance with NASA policy the International System of Units (SI Units), as defined in NASA SP-7012, are used in this publication.

The papers in this report were presented May 28, 1970

William G. Johnson
Director
Research Planning Office

PRECEDING PAGE BLANK NOT FILMED

CONTENTS, . . .

STATISTICAL DETERMINATION OF SAFETY FACTOR REQUIREMENTS FOR UNTESTED
STRUCTURES FROM SATURN V TEST DATA

By Jerrell M. Thomas

| | Page |
|---------------------------------------|------|
| INTRODUCTION. | 1 |
| DESCRIPTION OF METHOD. | 1 |
| SATURN V TEST DATA ANALYSIS | 2 |
| CONCLUSIONS. | 4 |

LIST OF TABLES

| Table | Title | Page |
|-------|-----------------------------|------|
| 1. | Saturn V Test Data. | 2 |

LIST OF ILLUSTRATIONS

| Figure | Title | Page |
|--------|---|------|
| 1. | Schematic of failure frequency distributions | 1 |
| 2. | Saturn V test data — histogram and normal distribution | 3 |
| 3. | Predicted failure distribution of untested Saturn V type structures | 3 |
| 4. | Failure probability prediction. | 4 |
| 5. | Equivalent safety factors | 4 |

MODAL ANALYSIS OF STRUCTURES BY AN ITERATIVE RAYLEIGH-RITZ TECHNIQUE

By John R. Admire

| | Page |
|----------------------------------|------|
| SUMMARY | 5 |
| INTRODUCTION. | 5 |
| ANALYTICAL DEVELOPMENT | 6 |

CONTENTS (Continued) . . .

| | Page |
|-----------------------------|------|
| NUMERICAL RESULTS | 7 |
| CONCLUSIONS | 10 |
| REFERENCES | 11 |

LIST OF ILLUSTRATIONS

| Figure | Title | Page |
|--------|---|------|
| 1. | Frame structure | 8 |
| 2. | Plot of the square of the frequency versus the number of iterations | 8 |
| 3. | Rate of convergence of frequencies where the initial frequencies are greatly in error | 9 |
| 4. | Mode shape of third mode | 10 |
| 5. | Plot of the square of the frequency versus the number of iterations with the coordinate vectors generated arbitrarily | 11 |

FLOW INDUCED VIBRATIONS IN METAL BELLOWS

By H. J. Bandgren

| | Page |
|--|------|
| SUMMARY | 13 |
| INTRODUCTION | 13 |
| VORTEX SHEDDING FROM BELLOWS CONVOLUTIONS, THE FLOW EXCITATION MECHANISM | 13 |
| SEMIEMPIRICAL METHOD FOR ESTIMATING FLOW INDUCED DYNAMIC STRESSES IN METAL BELLOWS | 16 |
| METHODS OF ELIMINATING OR MINIMIZING FLOW INDUCED DYNAMIC STRESSES | 20 |
| CONCLUSIONS | 20 |
| BIBLIOGRAPHY | 21 |

LIST OF ILLUSTRATIONS

| Figure | Title | Page |
|--------|-----------------------------------|------|
| 1. | Vortex shedding process | 14 |

CONTENTS (Continued) . . .

| | Page |
|--|------|
| 2. Bellows stress as a function of flow rate for four flow excited modes of vibration | 14 |
| 3. Observed bellows longitudinal vibration mode shapes | 15 |
| 4. Metal hose flow excited vibration mode | 15 |
| 5. Two-dimensional bellows flow visualization model. | 16 |
| 6. Sequence of coupled fluid-convolution events observed with two-dimensional bellows flow visualization model. | 17 |
| 7. Illustration of stress resulting from vortex force. | 17 |
| 8. Diagram of convolution vibration test model and equivalent bellows and mechanical model representations | 17 |
| 9. Summary of bellows vortex force coefficient experimental data | 18 |

NASTRAN, NASA'S GENERAL PURPOSE STRUCTURAL ANALYSIS PROGRAM

| | Page |
|----------------------------|------|
| By R. L. McComas | 23 |

LIST OF ILLUSTRATIONS

| Figure | Title | Page |
|--------|---|------|
| 1. | Dished head assembly drawing | 25 |
| 2. | Finite element model of ATM solar array. | 25 |
| 3. | Finite element model of dished head assembly. | 25 |

SKYLAB DOCKING RESPONSE ANALYSIS

By W. B. Holland

| | Page |
|---------------------------|------|
| ABSTRACT. | 27 |
| INTRODUCTION. | 27 |
| PHYSICAL PROBLEM. | 28 |

CONTENTS (Continued) . . .

| | Page |
|----------------------------------|------|
| ANALYTICAL DEVELOPMENT | 28 |
| EQUATIONS OF MOTION. | 28 |
| STATE VECTOR | 30 |
| CONSTRAINT CRITERIA | 32 |
| NUMERICAL EXAMPLE | 32 |
| REFERENCES. | 34 |

LIST OF TABLES

| Table | Title | Page |
|-------|---|------|
| 1. | Description of the Constraints. | 32 |

LIST OF ILLUSTRATIONS

| Figure | Title | Page |
|--------|--|------|
| 1. | Skylab docking configuration. | 27 |
| 2. | Docking system major assemblies. | 28 |
| 3. | Probe docking system. | 29 |
| 4. | Coordinate systems | 31 |
| 5. | Probe mechanism geometry. | 32 |
| 6. | Docking force time history. | 33 |
| 7. | Docking force time history. | 34 |

PAYLOAD ENCLOSURE NOISE REDUCTION

By B. E. Erwin

| | Page |
|--------------------------------|------|
| INTRODUCTION. | 35 |
| DEFINITION OF PROBLEM. | 35 |
| PROPOSED SOLUTION | 35 |
| TEST PROCEDURE | 36 |
| DATA REDUCTION. | 38 |
| TEST RESULTS. | 38 |

CONTENTS (Continued) . . .

| | Page |
|----------------------|------|
| CONCLUSIONS. | 40 |
| REFERENCES. | 40 |

LIST OF ILLUSTRATIONS

| Figure | Title | Page |
|--------|---|------|
| 1. | Skylab enclosure designs | 35 |
| 2. | Comparison of noise reduction for SLA and skin-stringer enclosure | 36 |
| 3. | Typical test setup. | 37 |
| 4. | Noise reduction of a monocoque cylinder in a reverberant acoustic field | 38 |
| 5. | Noise reduction of a monocoque cylinder in a reverberant acoustic field | 39 |
| 6. | Noise reduction of a monocoque cylinder in a reverberant acoustic field | 40 |

S-II STAGE VIBRATION TESTING AND ANALYSIS FOR THE POGO PHENOMENA

By H. M. Lee

| | Page |
|--|------|
| SUMMARY | 41 |
| INTRODUCTION. | 41 |
| DESCRIPTION OF TESTS | 41 |
| MATH MODELING TECHNIQUE | 43 |
| COMPARISON OF TEST AND MODEL DATA. | 45 |
| COMPARISON OF VEHICLE ANALYSIS AND FLIGHT DATA | 46 |
| CONCLUSIONS. | 47 |
| REFERENCE. | 48 |

LIST OF TABLES

| Table | Title | Page |
|-------|--|------|
| 1. | Comparison of Actual Weights with Weights Calculated from Mass Matrices. | 46 |

CONTENTS (Concluded)...

| | Page |
|--|------|
| 1. AS-504 vibration amplitudes..... | 42 |
| 2. S-II oscillation overall program flow..... | 43 |
| 3. Test definition..... | 44 |
| 4. Phase I frequency versus time..... | 44 |
| 5. Phase II and III frequency versus time..... | 45 |
| 6. Phase I — model/test comparison..... | 46 |
| 7. Phase II — model/test comparison..... | 46 |
| 8. S-II flight model..... | 47 |
| 9. Flight data versus flight model..... | 48 |

STATISTICAL DETERMINATION OF SAFETY FACTOR REQUIREMENTS FOR UNTESTED STRUCTURES FROM SATURN V TEST DATA

By

Jerrell M. Thomas

INTRODUCTION

A traditional method of assuring structural reliability in aircraft, missiles, spacecraft, and launch vehicles is the application of structural safety factors. These safety factors must always be carefully defined to meet the needs of the particular system; but for our purposes, it is sufficient to define the safety factor as the ratio of the load required to produce failure in a structure to the maximum expected load in service (limit load). Typical safety factors in the aerospace industry range from 1.2 to 1.5 for major structures. It is standard practice to test a specimen of every major structure to assure that the required safety factors do exist.

The increasing size and complexity of aerospace structures, coupled with the more complex combinations of environments, cause the cost of testing and the influence of the testing on overall development schedules to continually increase. This provides sufficient motivation to search for ways to minimize the test program. Is it possible to decrease the scope of required testing to gain cost and schedule advantages without sacrificing the all important system reliability? In the large systems of the immediate future, such as the Space Shuttle and Space Station, certain structures will almost certainly be sized by stiffness requirements from dynamic considerations or by long life requirements. Thus, these structures may have an inherently large safety factor on the maximum expected load. In other systems, it may be feasible to increase the safety factor to some desired level at the expense of adding weight. The purpose of this paper is to illustrate a possible method for determining what safety factor is required to provide reliable structures without testing.

DESCRIPTION OF METHOD

There will always be inaccuracies in predicting the failure load of any given structure. It is reasonable to expect that the failure load will be overpredicted in some cases and underpredicted in others, with most structures failing near the predicted value and with

a decrease in the probability of failure at load levels either above or below the predicted level. As will be shown later, the distribution of failure frequency about a mean value (near the predicted value) is approximately normal for Saturn V structures. This is illustrated schematically in Figure 1a. Design changes are usually made in those structures that fail at less than the predicted level while those that fail at or above the predicted level are left unchanged. As a result, the failure frequency of structures that are actually used in flight would appear somewhat as illustrated in Figure 1b. This odd distribution would

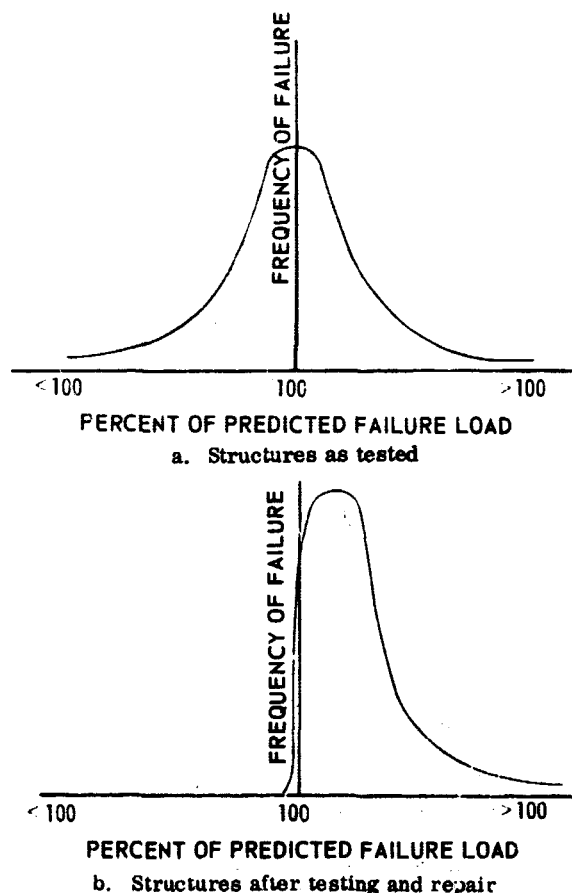


Figure 1. Schematic of failure frequency distributions.

then make a statistical prediction of probability of failure in flight very difficult, even if other important variables such as manufacturing differences and expected load uncertainties are ignored.

The concern of the present analysis is to accomplish the somewhat easier task of determining the safety factor for untested structures that will give essentially the same probability of success as that obtained with tested structures. This is accomplished by first assuming that the Saturn V structure is representative of the structural article under consideration. Statistical properties of the Saturn V test can be determined, and a normal distribution curve similar to Figure 1a can be constructed. Once this is done, a percentage of the predicted failure load can be determined for which a selected probability exists that the failure load of the article under consideration will exceed. From this percentage, the required safety factor can be determined to assure that the structural article will not fail at less than the ultimate load.

SATURN V TEST DATA ANALYSIS

Assumptions and Limitations

It is assumed that all structural components can be grouped statistically and that all tests were valid with respect to loads and environments. If a test specimen was not tested to failure, the maximum load sustained is taken as the strength of the specimen. If one test specimen was tested to a series of ultimate tests, the maximum load sustained in any test is taken as the strength.

Data Analyzed

A sample of the Saturn V test data that were analyzed is shown in Table 1. Basically, each data point represents one major Saturn V structural assembly such as a tank, interstage, or thrust structure. In some cases structural articles were subjected to more than one load condition. If these load conditions were very similar to each other, the maximum load sustained in any test was taken as the specimen strength. In other cases a single structural article was subjected to more than one test, and the test conditions were entirely different. In these cases more than one data point was gained from the single structural assembly.

TABLE 1. SATURN V TEST DATA

| Data Point Number | Test Safety Factor | Percent of Predicted | Tested to Failure |
|-------------------|--------------------|----------------------|-------------------|
| 1 | 1.40 | 100 | No |
| 2 | 1.58 | 113 | Yes |
| 3 | 1.12 | 60 | Yes |
| 4 | 1.65 | 118 | Yes |
| ⋮ | ⋮ | ⋮ | ⋮ |
| ⋮ | ⋮ | ⋮ | ⋮ |
| ⋮ | ⋮ | ⋮ | ⋮ |
| ⋮ | ⋮ | ⋮ | ⋮ |
| 50 | 1.41 | 101 | Yes |

Most of the Saturn V structures are made from high strength aluminum materials. The construction is a mixture of riveted skin-stringer, integrally stiffened, and sandwich articles.

The second column in Table 1 shows the safety factor attained by each article in the static structural test. This factor represents the ratio of the load attained in test to the limit load. The third column, which is the actual data analyzed, represents the percentage of the predicted capability load attained by the article. For purposes of this analysis, the predicted capability was taken as the limit load times the safety factor requirement for the article. An indication as to whether or not the article was tested to failure is given in the last column. Slightly more than half of the structures tested were tested to failure. The fact that some structures were not tested to failure produces an undesirable bias in the data, but this is not believed to be severe because many of the articles that did not fail were very near failure based on strain gage instrumentation.

Statistical Representation of Data

A statistical representation of the data is shown in Figure 2. The normal distribution was calculated by standard statistical methods. The histogram is shown to give a visual comparison of the actual data to the normal distribution curve. The data have a mean value of 0.99 and a standard deviation of 0.142. A more detailed representation of the statistical properties is shown in Figure 3. An example of conversion of the abscissa to any desired safety factor is shown on the (B) scale in Figure 3.

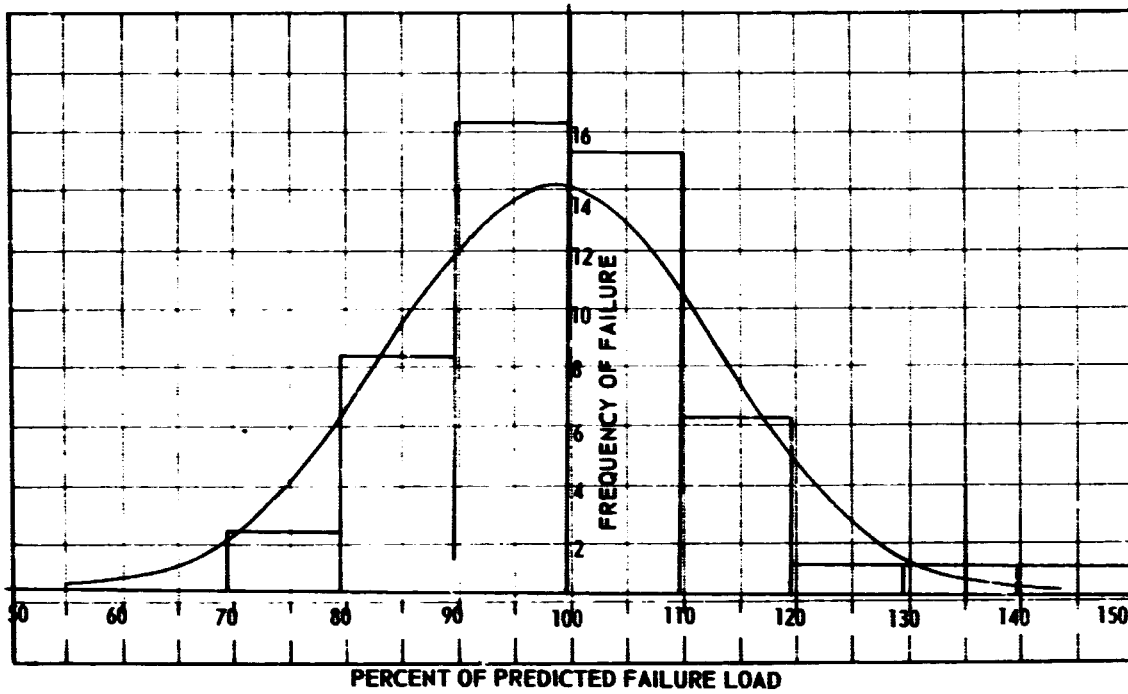


Figure 2. Saturn V test data — histogram and normal distribution.

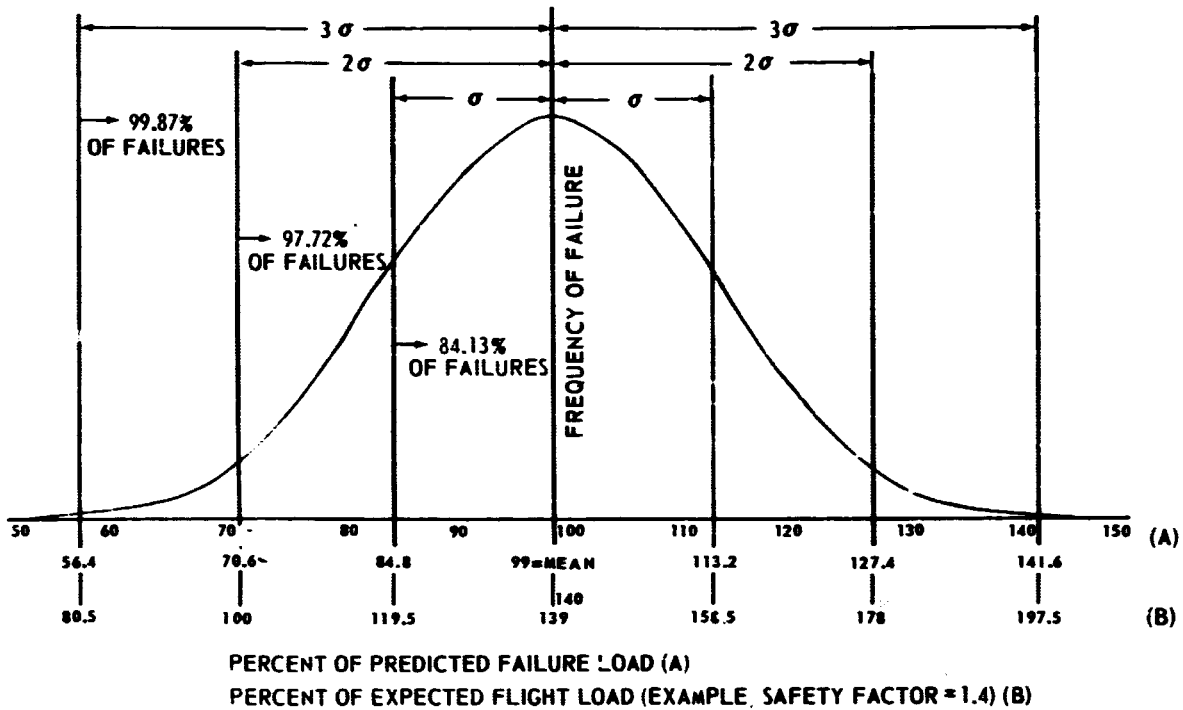


Figure 3. Predicted failure distribution of unterte: Saturn V type structures.

Analysis of Data

Let μ represent the mean of the test data. Then, the percentage of the expected failure load, which is Z standard deviations less than the mean value, is $\mu - Z\sigma$, where σ is the standard deviation. Thus, for untested structures, the ratio of the expected failure load to the actual failure load for a $Z\sigma$ probability is given by

$$R = \frac{100}{\mu - Z\sigma}$$

Then any desired value of failure load must be multiplied by this ratio to obtain a design load that gives a $Z\sigma$ probability of no failure at the desired failure load. If the safety factor of tested structures is represented by FS_t , the equivalent safety factor,

FS_u , for untested structures would be given by

$$FS_u = R \times FS_t$$

In Figure 4, the required safety factor, FS_u , for untested structures has been plotted versus the probability of no failure, $Z\sigma$, for various values of FS_t as a parameter. It should be noted that the $FS_t = 1.00$ plot (represented by the 100 percent limit load curve) gives the probability of failure for untested Saturn V type structures at limit load. Figure 5 is a crossplot of Figure 4 from which the equivalence between safety factors for tested and untested structures can be determined directly for either a 2σ or 3σ probability of no failure.

CONCLUSIONS

Although the data presented should not be interpreted as absolute because of the assumptions made and the limited test data available, they seem to yield a rational guide for choosing safety factors for untested structures. For structures sized by stiffness considerations, life requirements, or minimum gage restraints or for structures for which weight is not of utmost importance, a no-test philosophy with larger analytical safety factors to provide equivalent reliability is worthy of careful consideration.

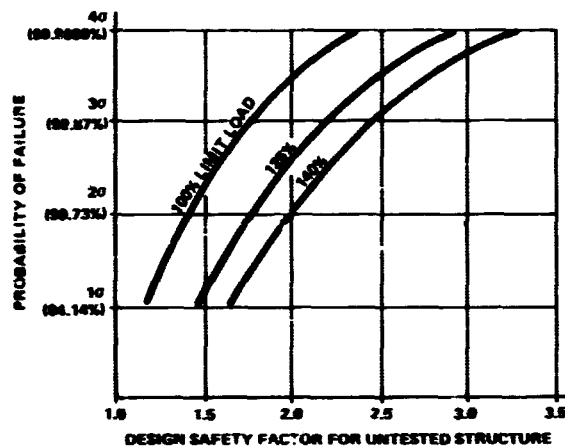


Figure 4. Failure probability prediction.

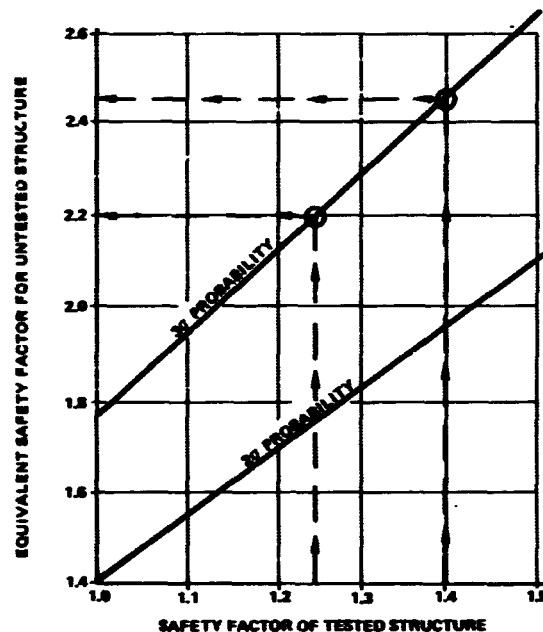


Figure 5. Equivalent safety factors.

MODAL ANALYSIS OF STRUCTURES BY AN ITERATIVE RAYLEIGH-RITZ TECHNIQUE

By

John R. Admire

SUMMARY

A method of modal analysis of structures is presented. The method is based on repeated applications of the well known Rayleigh-Ritz technique using improved coordinate vectors for each iteration. This procedure is convergent, since each application of the Rayleigh-Ritz technique yields a better approximation of the modal properties of the structure. Numerical examples are used to demonstrate the rapid convergence of the method.

INTRODUCTION

Dynamic response analyses are important in the design of elastic structures subjected to time-dependent applied forces, because the loads associated with these responses can exceed the loads from all other sources. The dynamic response of a structure is determined by solving its equations of motion. The present practice in the aerospace industry is to simulate the actual structure with a discrete coordinate model to obtain the equations of motion. The discrete coordinate equations of motion that result are coupled second-order differential equations. Since coupled differential equations are rather difficult to solve, they are transformed to a set of uncoupled differential equations. The transformation is accomplished using the mode shapes from a modal analysis, and the uncoupled equations are called modal equations. Thus, the most important use of data from a modal analysis is to simplify the dynamic response analysis.

The modal analysis of a discrete coordinate model of a structure having n degrees of freedom requires the solution of an n th-order matrix eigenvalue problem. A digital computer is usually used to solve the eigenvalue problem. The three most important items to consider when choosing a method to solve the eigenvalue problem on a computer are accuracy of the solution, computation time required, and computer storage required. There are many algorithms available for direct solution of the matrix eigenvalue problem [1]; however, as the number of degrees of

freedom becomes large, the computation time and computer storage becomes excessive for most of these methods.

The technique most often used in the aerospace industry to reduce the computation time and computer storage to acceptable levels for modal analysis is the Rayleigh-Ritz method [2]. This method permits an approximation of the first m modes of the structure to be obtained by solving an m th-order eigenvalue problem rather than the original n th-order eigenvalue problem. Thus, when the number of modes desired is significantly less than the number of degrees of freedom of the model, a great deal of computer time and computer storage can be saved by using this method. The reduction in the order of the eigenvalue problem is accomplished by approximating the displacements of the discrete coordinates by a linear sum of m Rayleigh-Ritz coordinate vectors.

The theory on which the Rayleigh-Ritz method is based places only minor restrictions on the coordinate vectors that can be used. Thus, an analyst has great freedom in the choice of the coordinate vectors. When the coordinate vectors are derived from the modal properties of the components of the structure, the technique is called "modal coupling" or "component mode synthesis". The most well known method based on component modal properties is due to Hurty [3].

The inherent problem in using the Rayleigh-Ritz method is the accuracy of the approximate solutions. That is, in general it is necessary to use more Rayleigh-Ritz coordinate vectors than the number of modes desired in order to obtain sufficient accuracy. This procedure tends to defeat the purpose of the Rayleigh-Ritz method since the order of the eigenvalue problem is equal to the number of coordinate vectors rather than the number of modes desired.

The accuracy problem associated with the Rayleigh-Ritz method can be eliminated by applying the method repeatedly and using improved coordinate vectors each time. This procedure will converge to the exact modes since each application of the Rayleigh-Ritz method will yield a closer approximation of the exact modes of the structure.

Bajan, Feng, and Jaszlics [4] have suggested an iterative method and applied it using coordinate vectors derived from component modal properties. The iterative method presented here appears to converge more rapidly than the method of Bajan, Feng, and Jaszlics, at least for the example in their paper.

ANALYTICAL DEVELOPMENT

Consider a discrete coordinate model of a constrained structure having n degrees of freedom. The free, undamped equations of motion of such a model expressed in matrix notation are:

$$[M]\{\ddot{X}\} + [K]\{X\} = \{0\}, \quad (1)$$

where $\{X\}$ is a vector of discrete coordinate displacements, $[M]$ is the mass matrix, and $[K]$ is the stiffness matrix. The time dependence in equation (1) can be removed by the transformation $\{X\} = e^{i\omega t}\{X\}$, since its solutions are harmonic in time. Thus, equation (1) becomes

$$([K] - \omega^2 [M])\{X\} = \{0\}. \quad (2)$$

Equation (2) is recognized as a matrix eigenvalue problem of order n whose eigenvectors, $[Y]$, are the mode shapes and whose eigenvalues, $[\omega^2]$, are the squares of the frequencies.

The first step in using the Rayleigh-Ritz technique [2] to obtain approximate solutions of equation (2) consists of selecting a complete sequence of coordinate vectors

$$\{Z\}_1, \{Z\}_2, \dots, \{Z\}_m, \dots, \{Z\}_n, \quad (3)$$

which are linearly independent and satisfy the kinematic boundary conditions. The displacement vector $\{X\}$ is then expressed as a linear sum of the first m coordinate vectors

$$\{X\} = \sum_{j=1}^m q_j \{Z\}_j. \quad (4)$$

In matrix notation, equation (4) can be expressed as

$$\{X\} = [Z]\{q\}. \quad (5)$$

It is known from energy considerations [2] that the function

$$\omega^2 = \{X\}^T [K] \{X\} / \{X\}^T [M] \{X\} \quad (6)$$

must be stationary. The equations that will yield ω^2

stationary are obtained by expressing equation (6) in terms of $\{q\}$, differentiating it with respect to the Rayleigh-Ritz coordinates, q_j , and setting the result equal to 0; i. e.,

$$\frac{\partial \omega^2}{\partial q_j} = 0, \quad j = 1 \text{ to } m. \quad (7)$$

Performing the operations indicated by equation (7) yields

$$([Z]^T [K] [Z] - \omega^2 [Z]^T [M] [Z])\{q\} = \{0\}. \quad (8)$$

Equation (8) is a matrix eigenvalue problem of order m whose eigenvectors are $[y^*]$ and whose eigenvalues are $[\omega^2]$. The approximate mode shapes are obtained from the relationship

$$[Z] = [Z][Y^*]. \quad (9)$$

The accuracy of the mode shapes and frequencies obtained from the Rayleigh-Ritz method depends entirely on the coordinate vectors, $[Z]$. In general, there are no procedures available for choosing a set of coordinate vectors that will yield exact solutions. However, it is possible to state characteristics such a set must possess. Since the mode shapes derived from the method are a linear combination of the coordinate vectors, it is clear that exact modes would result if each coordinate vector was a linear combination of the first m mode shapes of the structure. Another way of stating this is that exact results would be obtained for the first m modes of the structure if the coordinate vectors did not contain any contribution of modes higher than m .

Consider an iterative procedure to eliminate the accuracy problem associated with the Rayleigh-Ritz technique. If the Rayleigh-Ritz technique was repeatedly applied and if each time it was applied the coordinate vectors used would yield more accurate results than the previous set of vectors, it is clear that the iteration procedure would converge to the exact solution. The only problem with the iteration procedure is generating an improved set of coordinate vectors; that is, a set of vectors which will yield more accurate results than the previous set of coordinate vectors. Before an improved set of coordinate vectors can be generated, it is necessary to establish the characteristics such a set must possess.

From the discussion of the characteristics that a perfect set of coordinate vectors must possess, it is clear that an improved set of vectors is a set in which each vector contains less contribution from the higher modes than the corresponding vector in the previous set. Since the approximate mode shapes obtained by the Rayleigh-Ritz technique are a linear sum of the

coordinate vectors, it is possible to state the characteristics of an improved set of coordinate vectors in terms of a set of approximate mode shapes; that is, a set of coordinate vectors will be an improved set with respect to the previous set of vectors, if each vector contains less contribution from the higher modes than the corresponding mode shape derived from the previous set of coordinate vectors. Thus, an improved set of coordinate vectors can be generated by suppressing the contribution of the higher modes in the approximate mode shapes. The procedure for suppressing the contribution of higher modes is well known; in fact, it is the basis of the matrix iteration method [5] of modal analysis.

Consider generating a vector $\{f\}$ from a vector $\{s\}$ by the following equation:

$$\{f\} = [K]^{-1} [M] \{s\} \quad (10)$$

The vector $\{s\}$ can be expressed as a linear sum of the mode shapes of the structure

$$\{s\} = \sum_{j=1}^n \{y\}_j b_j \quad (11)$$

Combining equations (10) and (11) yields

$$\{f\} = \sum_{j=1}^n [K]^{-1} [M] \{y\}_j b_j \quad (12)$$

Since $\{y\}_j$ and ω_j must satisfy equation (2), the following relationship exists:

$$[K]^{-1} [M] \{y\}_j = \frac{1}{\omega_j^2} \{y\}_j \quad (13)$$

Therefore, equation (12) can be written as

$$\{f\} = \sum_{j=1}^n \frac{b_j}{\omega_j^2} \{y\}_j \quad (14)$$

Comparing equations (11) and (14), it is evident that the contribution of the higher modes in $\{f\}$ is less than in $\{s\}$, since the magnitude of ω_j^2 increases with j . Thus, an improved set of coordinate vectors can be obtained from the relationship

$$[Z] = [K]^{-1} [M] [Y] \quad (15)$$

It is not advisable to use equation (15) directly to compute $[Z]$ since $[K]^{-1}$ is, in general, a full matrix and requires a great deal of storage. Thus, equation (15) is replaced by two equations and $[Z]$ is determined by solving a set of simultaneous equations; that is,

$$[F] = [M] [Y] \quad (16)$$

and

$$[F] = [K] [Z] \quad (17)$$

Equations (16) and (17) can be solved efficiently for structures whose mass and stiffness matrices are banded by using methods based on Cholesky's square-root technique [6].

The equations necessary in applying the iterative Rayleigh-Ritz technique have been developed. The essential steps of the technique can be summarized as follows:

1. Select a set of coordinate vectors $[Z]$.
2. Form the eigenvalue problem expressed by equation (8).
3. Solve equation (8) to yield the eigenvectors $[Y^*]$ and eigenvalues $[\omega^2]$.
4. Compute a set of approximate mode shapes by equation (9).
5. Compute an improved set of coordinate vectors $[Z]$ by solving equations (16) and (17).
6. Return to step 2.

The iteration is halted when the mode shapes and frequencies have attained the desired accuracy.

NUMERICAL RESULTS

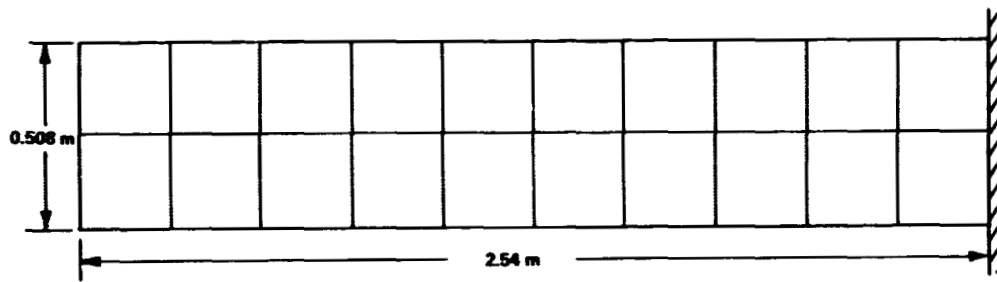
The preceding analysis was programmed for an IBM 7094 digital computer. Included in the program was a provision for computing static deflections resulting from unit loads applied at selected discrete coordinates. These static deflections were used as the initial coordinate vectors for the analysis.

Modal data were generated for the cantilever frame structure shown in Figure 1. The structure is composed of 50 identical members, each of which can deform axially and in bending. The axial stiffness, AE , bending stiffness, EI , and the mass density, ρ , of the members are also shown in Figure 1. A discrete coordinate model of the structure was generated using 3 degrees of freedom at each junction of the members, which resulted in a total of 90 degrees of freedom. The degrees of freedom used at the junctions were a rotation, a horizontal displacement, and

a vertical displacement. Modal data for this model were computed using a standard eigenvalue routine to verify the results obtained from the iterative Rayleigh-Ritz technique. The first three modes of vibration of this structure are primarily bending

modes, and the fourth mode is entirely an axial mode.

Figure 2 shows a plot of the square of the frequency versus the number of iterations. Also



THE DISCRETE COORDINATE MODEL OF THIS STRUCTURE HAS 3 DEGREES OF FREEDOM AT EACH JUNCTION FOR A TOTAL OF 90 DEGREES OF FREEDOM

BENDING STIFFNESS, $EI = 1.722 \times 10^2 \text{ N/m}^2$

AXIAL STIFFNESS, $AE = 2.135 \times 10^5 \text{ N}$

MATERIAL DENSITY, $\rho = 1.069 \times 10^4 \text{ N-sec}^2/\text{m}^4$

Figure 1. Frame structure.

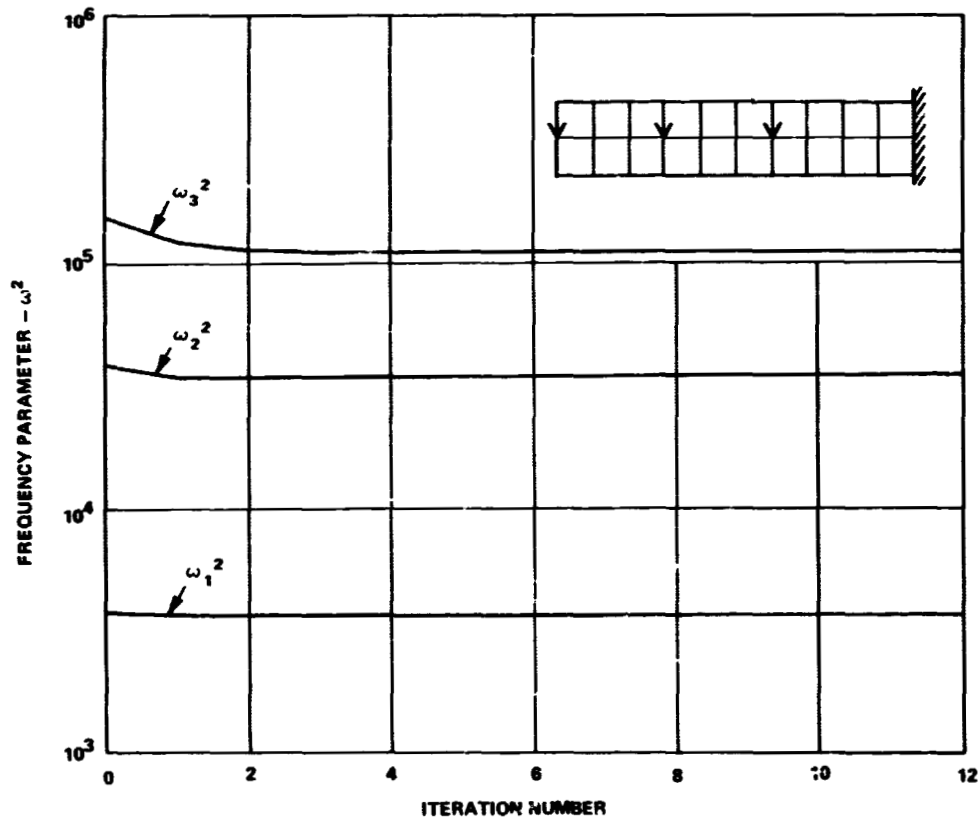


Figure 2. Plot of the square of the frequency versus the number of iterations.

shown in this figure is a sketch showing the structure with three arrows on it indicating the locations at which unit loads were applied to obtain the coordinate vectors. Since three coordinate vectors were used, three frequencies were obtained. They are shown plotted with a subscript indicating the mode number. The values of the frequencies shown for the 0th iteration are the frequencies computed from the initial set of coordinate vectors. All three frequencies converged to a constant value after three iterations with the third frequency requiring the most iterations since it was initially in error the most. From Figure 2 one could conclude that if the initial frequencies are not greatly in error, the technique produces rapid convergence. The next question that must be answered is: if the initial frequencies are greatly in error, will the technique still converge to the correct solution rapidly?

The purpose of Figure 3 is to show the rate of convergence of the frequencies for the case where

the initial frequencies are greatly in error. This figure is similar to Figure 2 except that a different set of initial coordinate vectors was used. The locations of the unit loads used to generate the coordinate vectors are shown as arrows in the figure. These initial coordinate vectors yielded frequencies that were as much as two orders of magnitude in error. The technique still yielded accurate solutions after only four iterations. Thus, one could conclude from Figures 2 and 3 that the number of iterations required to obtain accurate solutions does not depend greatly on the initial set of coordinate vectors.

Thus far, only the convergence of the frequencies has been discussed. The rate of convergence of the mode shapes is also important. Figure 4 shows the rate of convergence of the mode shape corresponding to the third frequency shown in Figure 3. This mode was selected since its frequency converged the slowest of the three shown

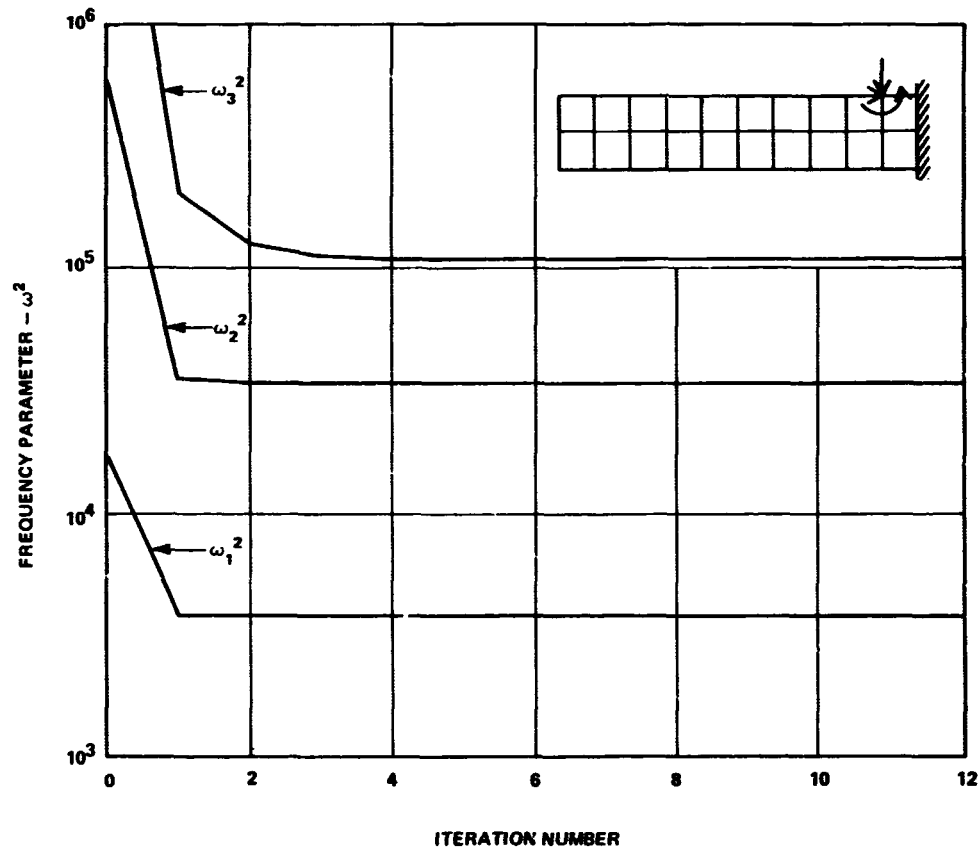


Figure 3. Rate of convergence of frequencies where the initial frequencies are greatly in error.

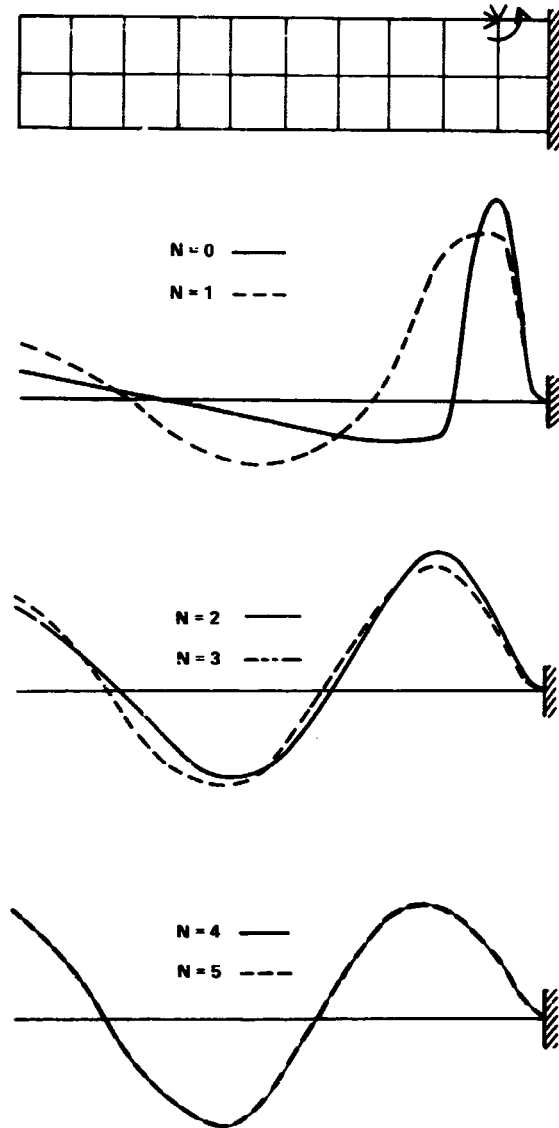


Figure 4. Mode shape of third mode.

in Figure 3. Figure 4 shows a plot of the centerline mode shape for iterations from zero to five. The mode shapes for the fourth and fifth iterations are almost identical. This indicates that the mode converged to a very accurate value in four iterations. Thus, from the numerical examples shown, it is evident that the iteration techniques will yield accurate mode shapes and frequencies after very few iterations.

Figure 5 shows what can happen if the coordinate vectors are generated arbitrarily. Again, the squares of the frequencies are plotted versus the iteration number, and the static loads used to generate the coordinate vectors are shown on the sketch. In the previous examples, all of the static loads used to generate the coordinate vectors caused the structure to deform at least to some extent in bending. That is not the case in this example. The horizontal force shown in Figure 5 causes no deformation normal to the centerline of the structure. Thus, the coordinate vector obtained from the horizontal force gives no approximation of the first three modes since they are bending modes. Figure 5 shows that the frequencies converged to a constant value rapidly, but the value to which the third frequency converged is not the true third frequency but is the fourth frequency of the structure. As mentioned previously, the fourth mode is an axial mode. Thus, the coordinate vectors chosen must approximate, at least to some extent, the type of modes that are being computed. After eight iterations, roundoff errors caused this mode to pick up a small amount of bending. When this happened, the iteration technique amplified this bending and suppressed the axial deformation, and it quickly converged to the true third frequency of the structure. Thus, some care must be taken in the coordinate vectors.

CONCLUSIONS

Based on the numerical examples presented, it appears the iterative Rayleigh-Ritz technique is an efficient means of computing modal data for structures having banded mass and stiffness matrices if reasonable care is used in selecting the coordinate vectors.

Initial coordinate vectors obtained from static loads were only used to demonstrate the iteration technique, and it should not be concluded that they are the best ones to be used. It is most likely that initial coordinate vectors derived from the modal properties of the components of the structure would be a better choice.

Even though the technique as presented applies only to constrained structures, it can be applied to unconstrained structures with only minor modifications.

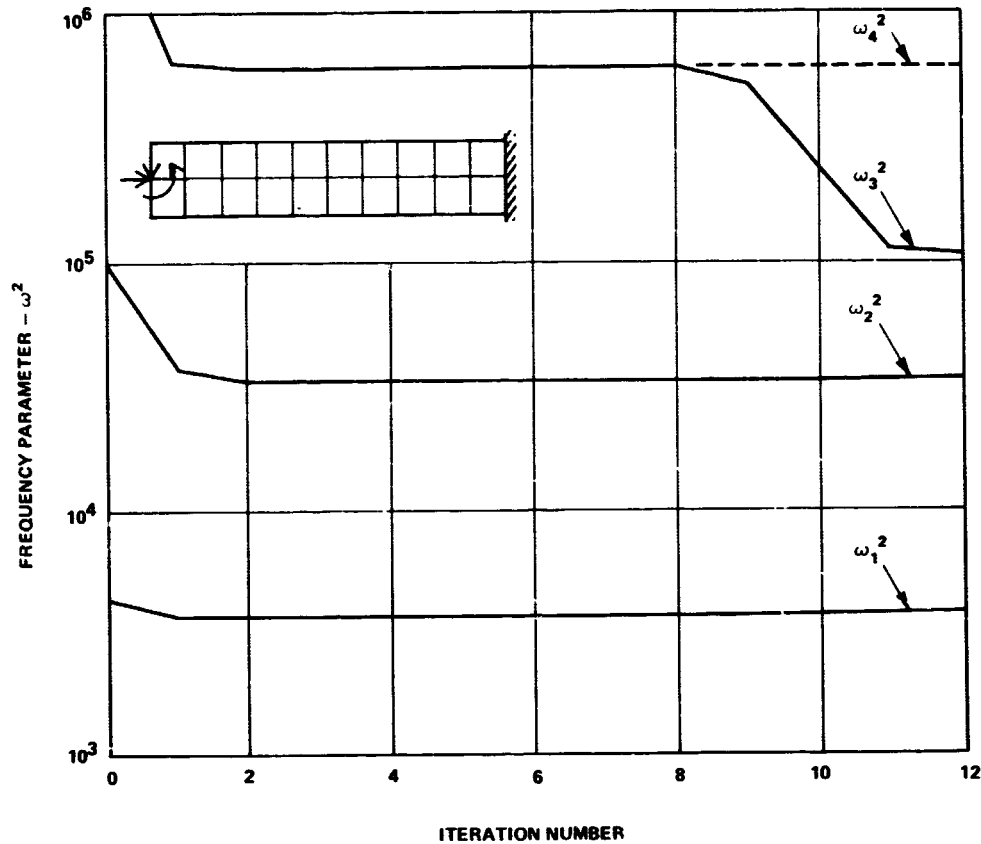


Figure 5. Plot of the square of the frequency versus the number of iterations with the coordinate vectors generated arbitrarily.

The most logical extension of this work would be to apply the iterative technique using initial coordinate vectors derived from the modal properties

of the structure's components and generate the improved coordinate vectors using substructuring techniques.

REFERENCES

1. Wilkinson, J. H.: The Algebraic Eigenvalue Problem. Clarendon Press, Oxford, 1965.
2. Mikhlin, S. G.: Variational Methods in Mathematical Physics. The MacMillan Company, New York, 1964.
3. Hurty, W. C.: Dynamic Analysis of Structural Systems by Component Mode Synthesis. Report 32-530, Jet Propulsion Laboratory, Pasadena, California, 1964.
4. Bajan, R. L.; Feng, C. C.; and Jaszlics, I. J.: Vibration Analysis of Complex Structural Systems by Modal Substitution. Proceedings of 39th Shock and Vibration Symposium, Monterey, California, October, 1968.
5. Hurty, W. C.; and Rubinstein, M. F.: Dynamics of Structures. Prentice-Hall, Inc., Englewood Cliffs, New Jersey, 1964.

REFERENCES (Concluded)

6. Wearer, W., Jr.: Computer Programs for Structural Analysis. D. Van Nostrand Company, Inc., Princeton, New Jersey, 1967.

FLOW INDUCED VIBRATIONS IN METAL BELLOWS

By

H. J. Bandgren*

SUMMARY

This paper summarizes the results of an experimental and analytical study of flow induced vibration of metal bellows. The results of numerous laboratory experiments have confirmed that vortex shedding from the tips of the bellows convolutions is the fluid excitation mechanism. When the frequency of the vortex shedding coincides with one of the natural longitudinal resonant frequencies of the free bellows or braided hose, a strong bellows vibration may exist.

A semiempirical method of estimating the flow induced dynamic stresses in a bellows for a given set of flow conditions has been formulated. Design methods for eliminating or minimizing the effects of flow induced vibration in bellows systems have been developed and experimentally verified.

The criteria presented in this paper were used to assess all of the metal bellows in the Saturn/Apollo launch vehicle system to determine if flow induced vibration problems existed. Corrective action was implemented where necessary by the installation of flow liners or the addition of damping to the bellows system.

INTRODUCTION

During the flight of the second Saturn V space vehicle, AS-502, one of the J-2 engines on the second stage malfunctioned causing the engine to shut down early. During the same flight the J-2 engine on the third stage failed to restart in earth orbit. More recently, during static firings of the S-IVB flight stages for AS-508 and AS-509, the LH_2 propellant delivery lines developed leaks. All of these anomalies were determined to be the result of flow induced vibration fatigue failures of the metal bellows.

This paper describes the results of an analytical and experimental study of flow induced vibrations in

metal bellows. A number of significant findings have been made throughout this study and are discussed in detail in the paper; these are listed below:

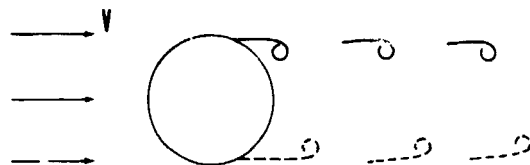
1. The fluid-elastic mechanism causing bellows flow excitation (vortex shedding) has been observed in the laboratory and is discussed.
2. A semiempirical method for estimating the flow induced dynamic stresses in a bellows for a given set of flow conditions is described.
3. Methods of eliminating or minimizing flow induced dynamic stresses are presented. Internal flow liners and various bellows external damping devices have been tried as a means of suppressing the bellows flow induced vibrations.

VORTEX SHEDDING FROM BELLOWS CONVOLUTIONS, THE FLOW EXCITATION MECHANISM

It is documented in the literature that when there is fluid flow over a cylinder, as shown in Figure 1, with a sufficiently high Reynolds number, a succession of alternately shed vortices will occur in the near wake region of the cylinder. Over a Reynolds number range of from 300 to 300 000, the frequency of the vortex shedding is related to the Strouhal number (S), flow velocity (V), and the diameter (D) of the cylinder as shown in Figure 1. This same phenomenon has been shown to occur when fluid flows through a bellows with open convolutes, as depicted at the bottom of Figure 1. The length quantity is σ , the width of the convolute.

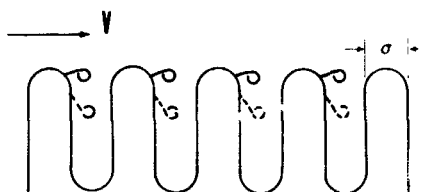
When the vortex shedding frequency of the bellows coincides with one of the longitudinal resonant frequencies of the bellows, a strong bellows vibration may result. To verify this, the response characteristics of numerous bellows were studied in the flow facility. Figure 2 shows the flow induced dynamic stress at the tip of the convolute for a typical free bellows. This is a single ply bellows with an inside diameter of 5.08 cm (2.0 in.) and a convolute width of 0.3175 cm (0.125 in.). A graph of root

* This study was performed in conjunction with Southwest Research Institute under contract NAS8-21133 with Dr. C. R. Gerlach as the principal investigator.



$$f = SV/D = 0.2 V/D$$

VORTEX SHEDDING FROM CYLINDER



$$f = SV/\sigma = 0.2 V/\sigma$$

VORTEX SHEDDING FROM BELLWS CONVOLUTIONS

Figure 1. Vortex shedding process.

mean square stress at the tip of the end convolution is plotted against flow rate in liters/sec (gallons per minute are also shown). As the flow rate increased, a succession of bellows modes were excited. Before the bellows was installed in the flow facility, it was filled with water, capped off, and fixtured on an electrodynamic shaker to identify its longitudinal natural frequencies. These were 400 Hz for the first mode, 780 Hz for the second mode, 1130 Hz for the third mode, and 1450 Hz for the fourth mode. The significance here is that the flow rate corresponding to each of the stress build-ups shown in Figure 2 resulted in a particular vortex shedding frequency that coincided with one of the longitudinal resonant frequencies of the bellows when a Strouhal number of approximately 0.2 was used in the calculation for the vortex shedding frequency. Also, the dynamic stress increased as the mode number increased, because the vortex shedding forces are proportional to the free-stream stagnation pressure, $\frac{1}{2} \rho V^2$ (where ρ is the fluid mass density).

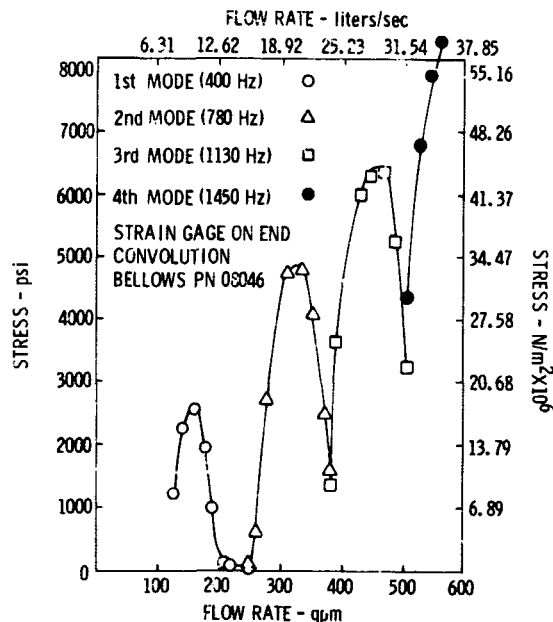


Figure 2. Bellows stress as a function of flow rate for four flow excited modes of vibration.

The type of longitudinal resonant modes that are excited in a free bellows are shown in Figure 3. These resonant modes are sometimes referred to as the accordion modes. For the first four natural modes of the previous bellows, axial displacement is plotted on the ordinate as a function of position along the bellows on the abscissa. The first natural mode is 400 Hz. There are nodes at the ends of the bellows, and all of the convolutions are moving in phase with the maximum motion at the center of the bellows. The second mode is 780 Hz. The nodes are at the center and end points of the bellows, and the maximum motion is at the quarter points 180 degrees out of phase. See Figure 3 for a description of the third and fourth modes.

A bellows vibrating in one of its accordion modes is better represented by a lumped parameter system than by a continuous system. The mechanical model shown at the bottom of Figure 3 was found to give quite adequate predictions of the longitudinal bellows frequencies. The model consists of a series of equal

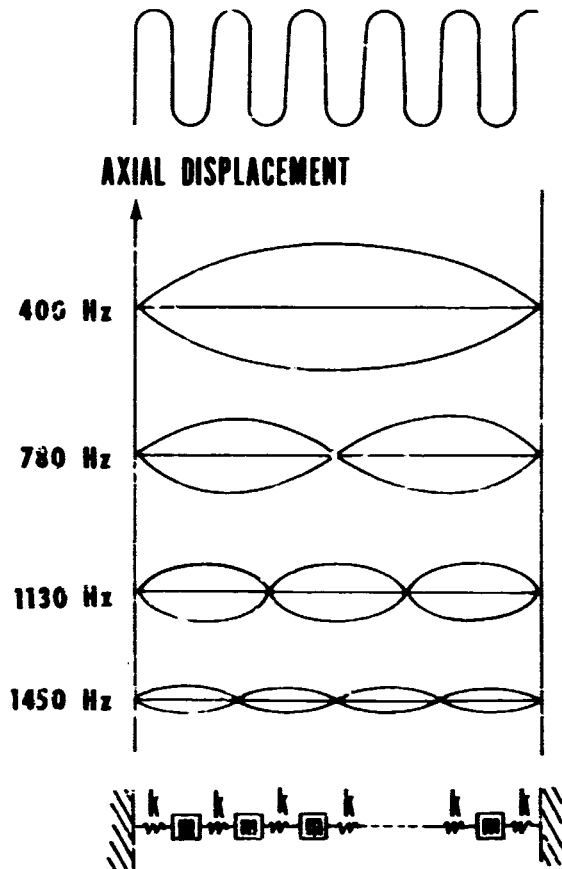
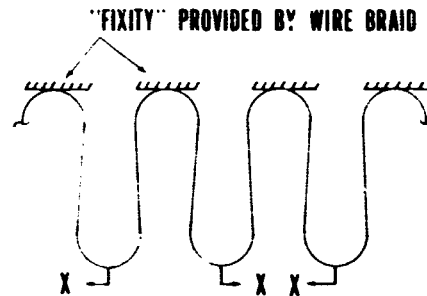


Figure 3. Observed bellows longitudinal vibration mode shapes.

springs (k) and masses (m) fixed at the ends. The individual springs can be determined from the axial spring rate of the bellows; the masses can be determined from the total mass of the bellows convolutions plus the mass of the fluid trapped in the root of the convolutes. The mass and flexibility matrices can be determined from the model, and any standard eigenfunction routine will provide the resonant frequencies and mode shapes.

For a braided hose the type of modes that are excited by the vortex shedding forces are shown in Figure 4. The adjacent crowns of the convolutes are fixed by the wire braid, and a simple cantilever mode of the individual roots of the convolutes is excited. These are sometimes referred to as reed modes, and the spring mass system is a simple one as shown at the bottom of Figure 4.

Experimental stroboscopic observations have been used to verify that these are the longitudinal



EACH CONVOLUTION MAY BE MODELED AS SHOWN BELOW.



Figure 4. Metal hose flow excited vibration mode.

bellows modes that are excited by the vortex shedding forces. To experimentally verify that vortex shedding is the mechanism that is exciting the longitudinal modes of the bellows, a model consisting of a two-dimensional clear plastic channel containing a short section of convoluted metal was constructed, as shown in Figure 5, and placed in the flow facility. As in an actual bellows, the convolution tips are exposed to the fluid flow. When water is passed through the channel at the proper flow velocity, the convolutions are flow excited. By injecting ink upstream from the convoluted segment and by slowing down the motion with the aid of a strobe light, the vortex shedding process was readily visualized, and motion pictures were taken.

Figure 6 shows the sequence of fluid and convolution events that were observed in a frame-by-frame examination of the motion pictures. Note that the mode of vibration of the segment is one where each convolution moves out of phase with the adjacent convolutions. The vortex shedding process on the vibrating convolution segment, as shown in Figure 6, occurs as follows:

1. Position I — A large vortex c has formed between convolutions 1 and 2. A small vortex b is beginning to form on the downstream side of convolution 2. A large vortex a is moving across the tip of convolution 3; its origin will become apparent later.

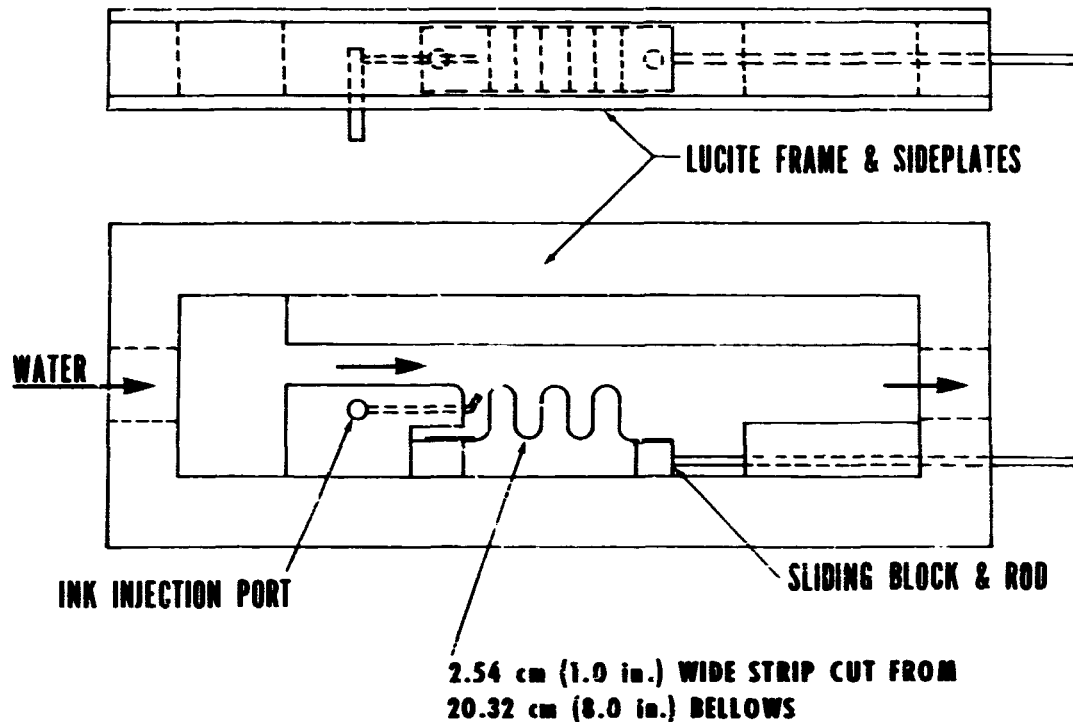


Figure 5. Two-dimensional bellows flow visualization model.

2. Position II — Vortex *c* has been pushed downstream by the pinching action of convolutions 1 and 2. Vortex *b* is gaining in strength on the downstream side of convolution 2. Vortex *a* is propagating downstream.

3. Position III — The space between convolutions 1 and 2 has opened up causing the fluid to be drawn in, and vortex *d* is beginning to form on the downstream side of convolution 1. Vortex *c* has been swept over the top of convolution 2 with the timing being about right to combine with vortex *b*, forming the larger vortex *b + c*.

4. Position IV — Vortex *d* is gaining in strength on the downstream side of convolution 1. Vortex *b + c* is being pushed out into the fluid stream by the "pinching" action of convolutions 2 and 3.

5. Position V — This is the same as position I completing one cycle of the vortex shedding process. Note that vortex *a* in position I is the combination of two vortices, as is *b + c* in position V.

SEMIEMPIRICAL METHOD FOR ESTIMATING FLOW INDUCED DYNAMIC STRESSES IN METAL BELLOWS

The previous discussion has been directed to the problem of when and how a bellows can be flow excited. The coincidence of the longitudinal resonant frequencies of a bellows with the vortex shedding frequency does not indicate the severeness of the vibration. During this study, an attempt has been made to predict vibration amplitudes and corresponding stress levels in a bellows for a given set of flow conditions.

Figure 7 shows the fluid and structural dynamics involved in bellows flow excitation. The process of periodic vortex formation and shedding causes a corresponding periodic pressure to be exerted on the bellows convolutions. The amplitude of this alternating pressure is proportional to the free-stream

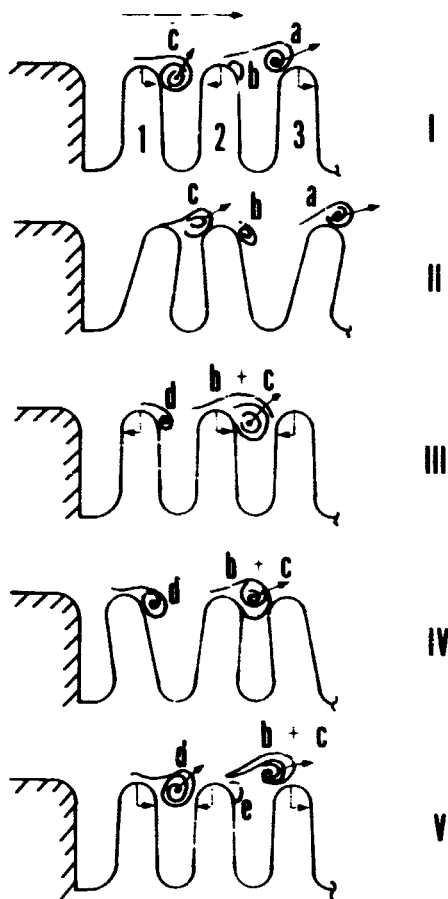


Figure 6. Sequence of coupled fluid-convolution events observed with two-dimensional bellows flow visualization model.

stagnation pressure $\frac{1}{2} \rho V^2$. So far as the bellows structure is concerned, the effect of this alternating pressure may be considered as a net force applied at the tip of each convolution. This force is called the vortex shedding force. The semiempirical equations for the vortex force, the convolution displacement, and the resulting stress at the tip of the convolution are shown in Figure 7.

Figure 8 shows the model that was used to determine the value of the vortex force coefficient C_F . A single bellows convolution was simulated in this test by a flexible steel ring clamped in a special housing between a pair of exciter coils. A displacement probe was built into the apparatus to allow ring vibration amplitudes to be monitored. The convolution vibration test model was placed in

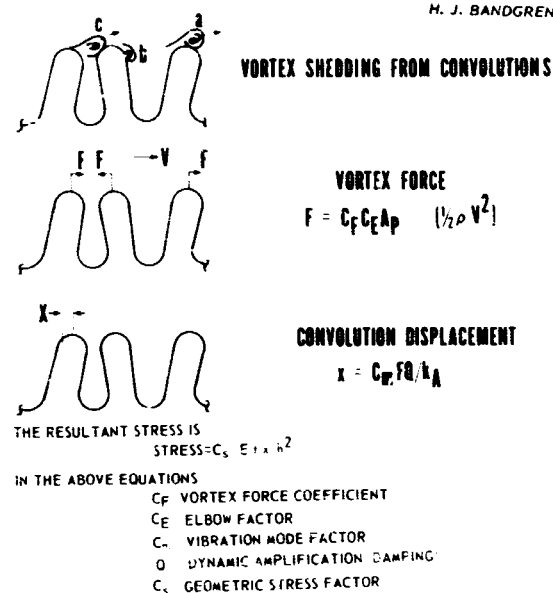


Figure 7. Illustration of stress resulting from vortex force.

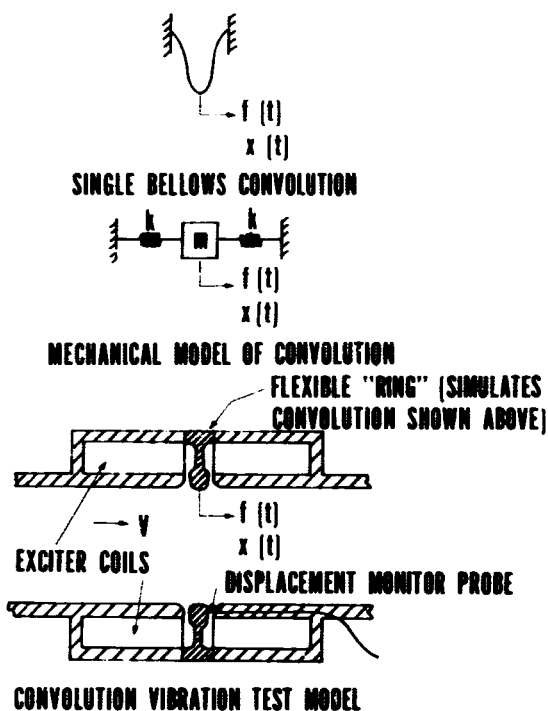


Figure 8. Diagram of convolution vibration test model and equivalent bellows and mechanical model representations.

the flow facility, and the vibratory response of the ring in water was determined with the excitation provided by the exciter coils. Next, the frequency response of the ring was determined with the fluid flow providing the excitation. Finally, a static force versus deflection calibration was made on the ring. The data from these tests were used as follows:

1. Vibration amplitude as a function of fluid velocity was converted to an apparent force using the data from the force-deflection calibration.
2. This apparent force was converted to a true vortex force by dividing it by the dynamic amplification factor Q , obtained from the forced vibration test in water.

3. The vortex force coefficient C_F was then determined from the equation for the vortex force shown in Figure 7.

Vortex coefficient data were obtained in this manner for several convolution geometries. They were also obtained from numerous tests on real bellows. The results of these tests are summarized in Figure 9. The vortex force coefficient C_F is plotted on the ordinate as a function of the ratio of pitch to convolute tip width on the abscissa. Notice the great reduction in the force coefficient as the convolution pitch is opened.

The next factor in the vortex force equation shown in Figure 7 is the elbow coefficient C_E . The

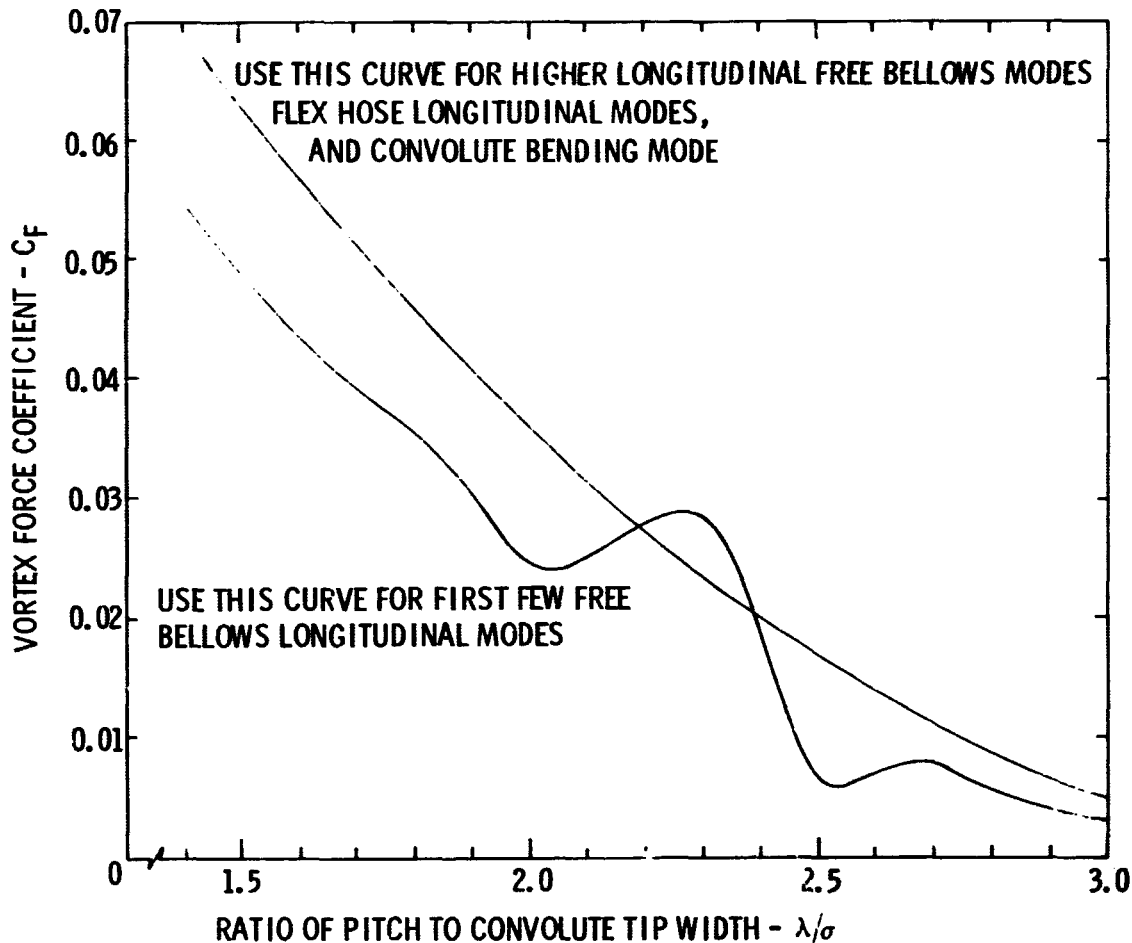


Figure 9. Summary of bellows vortex force coefficient experimental data.

presence of an elbow upstream from a bellows causes excessive flow induced dynamic stresses because of the increased turbulence. There is little quantitative data available on this effect, but the available data suggest correcting the vortex shedding force upward by a factor of 2.0 to account for the presence of an upstream elbow.

A_p is the projected area of the convolute and can be approximated by the product of the mean circumference and the height of the convolute. The final quantity in the vortex force equation is the free stream stagnation pressure $\frac{1}{2} \rho V^2$.

The convolution displacement resulting from the vortex force is shown in the second equation of Figure 7. The vibration mode factor C_m relates displacement and force for a given resonant condition. The following assumptions were made in the derivation of the vibration mode factor:

1. The shape of the longitudinal bellows modes is intermediate between a linear and sinusoidal form.
2. The maximum deflection for a given mode is equal to the static deflection times Q , the dynamic amplification factor.
3. The maximum stress point for a given vibration mode occurs at the convolution with the maximum relative displacement. Generally, this is the end convolution for each half-wave mode shape.

The first assumption implies that the mode shape over the first quarter wavelength is

$$x = \frac{x_0}{2} \left[\left(\frac{N}{l} \right) Y + \sin \left(\frac{\pi N Y}{l} \right) \right], \quad (1)$$

where x denotes the axial absolute displacement of a given point along the bellows defined by the axial position coordinate Y , N is the mode number, and l is the length of the bellows.

The second assumption implies that the maximum absolute displacement x_0 is

$$x_0 = \frac{FQ}{4NK_A}, \quad (2)$$

where F is the vortex shedding force, Q is the dynamic amplification factor, and K_A is the axial spring rate of the bellows.

From the third assumption, the point of maximum relative displacement x_{mr} for a given bellows, and a given mode of vibration, occurs at a point where $Y = l/2N_C$. Therefore, from equation (1)

$$x_{mr} = \frac{x_0}{2} \left[\frac{N}{N_C} + \sin \left(\frac{\pi N}{2 N_C} \right) \right]. \quad (3)$$

Combining equations (2) and (3) yields

$$x_{mr} = \frac{FQ}{8NK_A} \left[\frac{N}{N_C} + \sin \left(\frac{\pi N}{2 N_C} \right) \right], \quad (4)$$

and by comparison with the equation for the convolution displacement in Figure 7, the vibration mode factor C_m is

$$C_m = \frac{1}{8N} \left[\frac{N}{N_C} + \sin \left(\frac{\pi N}{2 N_C} \right) \right] \quad (5)$$

Returning now to the equation for the convolution displacement shown in Figure 7, the next factor is the vortex shedding force F that has been discussed and then the dynamic amplification factor Q , a measure of damping. Physically, Q represents the ratio of the vibration amplitude at resonance to the vibration amplitude in the limits of zero frequency. It also can be expressed as the resonant frequency divided by the frequency bandwidth at the half-power points for a given resonant buildup. Because Q is so important in the prediction of bellows flow induced dynamic stresses, a large number of tests were performed from which Q values could be obtained. Each bellows tested was installed in a special fixture that rigidly connected the end flanges. This was to insure that the vibration modes excited were the same as those excited by the vortex shedding forces. The bellows were then excited with an electrodynamic shaker with the output strain at the tip of the convolutes measured to obtain Q values. Some observations noted during this testing were as follows:

1. As the strain was increased, the damping increased and lowered the Q values.
2. Increasing the number of plies in a bellows increases the damping significantly.
3. Going from a low pressure gas to a high pressure gas or from a light liquid to a dense liquid increases the damping.

Some typical Q values as a function of number of plies and flow media are:

| No. Plies | Medium | Q Range |
|-----------|--------------------------------------|------------|
| 1 | Air or low pressure gases | 150 to 200 |
| 1 | High pressure gases or light liquids | 100 to 150 |
| 1 | Heavy liquids | 50 to 100 |
| 2 | Gases | 40 to 50 |
| 2 | Liquids | 30 to 40 |
| 3 | All | 20 to 40 |

The last factor in the convolution displacement equation is K_A the axial spring rate of the bellows.

The most accurate method for determining K_A is from load deflection tests in the laboratory. Probably the most accurate analytical method for determining bellows spring rate was developed by the Battelle Memorial Institute. This is a computerized method that provides for both linear and nonlinear elastic deformations. Most noncomputerized techniques use equations similar to those developed by F. Salzmann.

The last equation in Figure 7 is for the resultant stress at the tip of the bellows convolution. The stress is related to Young's modulus (E) and ply thickness (t) of the bellows material, and the height (h) and deflection of the convolute by a geometric stress factor C_s . Here again, the Battelle Memorial

Institute has obtained very good agreement between theoretical and experimental methods using a computer solution for the stress deflection relationship. However, the Salzmann equations for determining the stress in a bellows for a given convolution displacement compare favorably with the experimental test results.

METHODS OF ELIMINATING OR MINIMIZING FLOW INDUCED DYNAMIC STRESSES

The mechanism by which metal bellows are excited by flow induced vibration and a semiempirical method of estimating the resulting stresses have

been discussed. The question now is: how can these dynamic stresses be eliminated or minimized? The installation of an internal flow liner in a bellows will eliminate flow induced dynamic stresses, when the liner design covers all of the active convolutions. The cone shape of most liners allows angular movement of the bellows but produces a constriction, resulting in unwanted pressure drops.

A method for reducing the flow stresses in a bellows is to add damping to the bellows structure. This can be accomplished by the following methods:

1. Increasing the number of plies of the bellows.
2. Filling the convolutions with some visco-elastic material such as rubber or 3M strip-caulk.
3. Placing a soft metal spring in each of the bellows convolutions.
4. Tightly wrapping the exterior of the bellows with wire screen.

Experimental results show all of these methods afford a considerable amount of damping.

CONCLUSIONS

An examination of test results of flow induced vibrations of numerous bellows confirmed that vortex shedding from the bellows convolutions is the excitation mechanism. When the vortex shedding frequency coincides with one of the natural resonant modes of the bellows, a strong vibration may exist.

Tests results compare favorably with the semiempirical method presented in this paper for predicting the flow induced dynamic stresses. They also confirm that the external damping devices suppress flow induced vibrations of bellows.

The results of this study were used to assess all of the bellows on the Saturn/Apollo launch vehicle system to determine flow induced vibration susceptibility and to provide guidelines for all necessary corrective action.

BIBLIOGRAPHY

Gerlach, C. R. : Study of Minimum Pressure Loss in High Velocity Duct Systems. Quarterly Report No. 4, Contract NAS8-21133, Southwest Research Institute, May 1968.

Gerlach, C. R. : Study of Minimum Pressure Loss in High Velocity Duct Systems. Quarterly Report No. 5, Contract NAS8-21133, Southwest Research Institute, August 1968.

Aerospace Recommended Practice (ARP) No. 735. Society of Automotive Engineers Publications, 1966.

Gerlach, C. R. ; and Schroder, E. C. : Study of Minimum Pressure Loss in High Velocity Duct Systems. Interim Technical Report No. 1, Contract NAS8-21133, Southwest Research Institute, July 1969.

Trainer, T. M. ; Hulbert, L. E. ; Lestingi, J. F. ; Keith, R. E. ; et al: Technical Report No. AFRPL-TR-68-22. Battelle Memorial Institute, March 1968.

NASTRAN, NASA'S GENERAL PURPOSE STRUCTURAL ANALYSIS PROGRAM

By

R. L. McComas

NASTRAN is a general purpose digital computer program for the analysis of large complex structures. The acronym NASTRAN is formed from NASA structural analysis. During the annual review of NASA's research program in the area of structural dynamics in January 1964, it became apparent that there was considerable effort by many of the Centers to develop computer programs for structural analysis, designed to meet the particular needs of each of the Centers. It was suggested that perhaps a single program could meet all their needs. The Office of Advanced Research and Technology appointed a committee with representation from eight NASA Centers to study this possibility. Thus, the Ad Hoc Group on Computer Methods in Structural Analysis was formed.

After 6 months of investigation, the Ad Hoc Group reported to NASA Headquarters that there was no digital program in existence that had broad, uniform capabilities in the three interdependent disciplines of analytical mechanics, numerical methods, and computer programming. The Group did observe that there was considerable capability dispersed throughout the aerospace industry that had not been collected into a single program. They also found that there was a tendency toward proprietary secrecy that inhibited any exchange of information. Communication was further hindered by the lack of compatibility between the structural analysis programs of any two companies. The Ad Hoc Group recommended that NASA sponsor an entirely new program aimed at bringing together all the best structural analysis computer techniques in the state-of-the-art.

NASA Headquarters endorsed the recommendations of the Ad Hoc Group and commissioned them to prepare a set of specifications. Fortunately, the papers from the first Wright Field Conference, "On Matrix Methods in Structural Analysis", were available to consult. The following objectives of the specifications have now been established:

1. Organize the program to be general-purpose.
2. Embody a large three-dimensional structural capability.

3. Establish computer independence.
4. Provide for modification without cascading effects.
5. Build-in the maximum of user convenience.
6. Document all aspects to gain maximum visibility.

The contract to implement the NASTRAN specifications was awarded to Computer Sciences Corporation (CSC) with MacNeal Schwendler, Martin Baltimore, and later Bell Aerosystems Company as subcontractors. The quality of the NASTRAN program and its documentation is testimony to the purposefulness with which the members of the implementation team applied themselves. This team has often exceeded the state-of-the-art guidelines that were established. A few examples are the segment file allocator, the general input/output module, matrix decomposition with active columns, the inclusion of scalar nonlinearities in control of system dynamics, the generality in the plot module, and the development of the self-contained "inverse power with shifts" module for eigenvalue extraction. The overall design of the program has set a new standard for general purpose programs of any discipline. The framework used in NASTRAN can be disassociated from elastic structures and can be applied to other disciplines, because there are no semantic implications in the executive operations. The program abounds in service code, which threads through every step of the problem physics providing convenience to the analyst.

Many policy decisions had to be made as to the content of NASTRAN. The total framework of the program was considered to be the most important; the executive system had to be capable of managing problems unbounded by core, be compact in its space requirements, be able to restart problems, be able to operate efficiently over different computers, and still be maintainable.

It was decided that only basic finite elements would be included to deal with one- and two-dimensional elastic relationships such as beams, plates, and

axisymmetric shells. Economy of running time for the state-of-the-art elements was the determining factor in their selection. More sophisticated and new elements have appeared in the state-of-the-art since the inception of this program; these can easily be incorporated.

The decision was made to write a single program in Fortran IV with some exceptional areas to be written in assembly language. Fortran IV, version 13, in its various forms on different computers, seems to have stabilized as a language that will be current for a reasonably long time. More than 99 percent of the program is written in Fortran. The program is modular, so that updating is a matter of revamping material within a module without modifying its external appearances.

Hopefully, the framework that has been built has sufficient capability to serve a sizable portion of the large problems that currently exist in the structural analysis community. It is intended that new capability be added or outdated capability be replaced by augmenting or replacing modules. An entire chapter in the Programmer's Manual has been devoted to the topic of Modifications and Additions in anticipation of serving this particular activity. The traffic in the development of new and increasingly versatile elastic modules is expected to be the most active. As analysts increase their use of the program, their detailed needs will become better defined and the result will be that the traffic in "convenience code" will also be expected to increase. It is desired that all such new features be called to the attention of the NASTRAN Project so that these ideas and routines can be disseminated to a broad audience.

A computer program having all of the capabilities of NASTRAN will obviously be large, as NASTRAN is. In fact it is larger than the entire Univac 1108 Exec 8 System Program at the Marshall Space Flight Center Computation Laboratory.

The overall effectiveness of a general purpose program depends in large measure on how well the available programming techniques have been employed in the design of its organizational and control features. NASTRAN has a modular separation of functional capabilities organized under an efficient problem-independent executive system. This approach is absolutely essential for any complex multioperation, multifile application program.

Despite the modular separation, it is clear that modules cannot be completely independent since they

are all directed toward solution of the same general problem. In particular they must intercommunicate data between themselves. The executive routine separates system functions from problem solution functions. It establishes and controls the sequence of module execution according to options specified by the user; it establishes and communicates values of parameters for each module; it allocates files for all data blocks generated during program execution and performs input/output to auxiliary files for each module; and it maintains a full restart capability for restoring a program execution after either a scheduled or unscheduled interruption. The executive system is open-ended in the sense that it can accommodate an essentially unlimited number of functional modules, files and parameters.

The functional modules are those modules that perform the actual calculations. They belong to one of four categories; i. e., structural modules, matrix operations, utility modules, and user modules.

The structural modules are the main subprograms of NASTRAN. Some examples of structural modules, taken from the dynamic analysis, are real eigenvalue analysis, modal dynamic matrix assembler, transient dynamic response, and dynamic data recovery. The NASTRAN development team has made every effort to incorporate the very latest and best structural techniques to preserve accuracy and speed of solution.

Most difficulties in numerical analysis arise in connection with three basic implicit operations; matrix decomposition (or inversion), eigenvalue extraction, and integration of differential equations. The major difficulties that occur in the application of these operations to large problems are excessive computing time, error accumulation, and instability. Many methods that work well with small or moderate size problems are not acceptable for large problems. The method employed for matrix decomposition (triangle decomposition with active column) is especially important because of its extensive use as a base for the other two implicit operations. The method that is employed in the program takes maximum advantage of matrix sparsity and bandedness. The latter aspect is particularly important because of the enormous gain in efficiency that occurs when banding techniques are properly employed by the user in setting up problems for the displacement method.

In general, the solution time for a large structural analysis of any type can be greatly reduced by taking full advantage of the sparsity and bandwidth of the matrices that describe the structural problem.

Other means have been used to improve efficiency for large problems. These include storing sparse matrices in packed form.

The input/output options have been designed to be flexible in order to accommodate the analyst. The plot package is very versatile allowing a choice of orthographic, perspective, or stereoscopic X-Y curve plot. All or portions of the structure can be plotted with varying view, line weight, and color.

The explanation of any complex activity must be subdivided into phases or steps to be intelligible. In the case of a computer program for structural analysis, it is convenient to divide the total effort into a problem formulation phase and a problem solution phase. The beginning of the problem formulation phase occurs in the mind of the analyst. He contemplates, decides what he needs to know, and constructs a mathematical problem whose solution, he hopes, will provide relevant answers to his question. The range of choice in mathematical problem formulation provided by NASTRAN is, however rich in detail, limited to one basic approach; namely, the use of finite element structural models. The idealized structural model in NASTRAN consists of grid points to which loads are applied and at which degrees of freedom are defined. The grid points are connected by elements in the NASTRAN element library. The structural element is a convenient localizing concept for specifying many of the properties of the structure including material properties, mass distribution, and some types of applied loads.

A wide range of elastic elements including several forms of beams, triangular and quadrilateral plates, scalar elements, and special shell and axisymmetric solid elements have been included in the element library.

Anisotropic material properties may be employed in all plate elements. With modeling experience, there is no aerospace structure that cannot be accurately modeled by the NASTRAN elements. Some examples that are currently being solved by NASTRAN are the dished head assembly (Fig. 1) and the ATM solar panels (Fig. 2). The idealized model of the dished head assembly (Fig. 3) is formed by beams and triangular plates. The grid mesh has been increased in the area of interest, the intersection of the two surfaces. Since the assembly is symmetric, only half of the structure needs to be modeled.

Now, all that is left to be done is to fill out the NASTRAN data cards (a simple although sometimes tedious task) and choose the analysis type, of which there are twelve available. There are five rigid

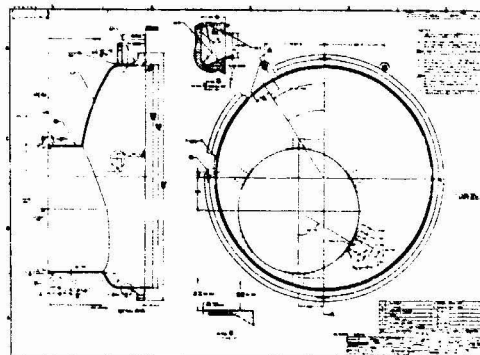


Figure 1. Dished head assembly drawing.

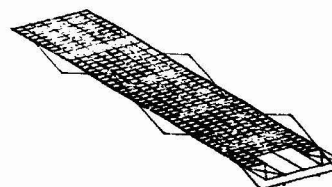


Figure 2. Finite element model of ATM solar array.

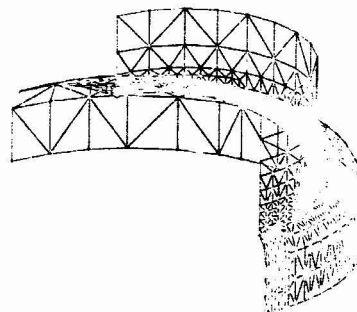


Figure 3. Finite element model of dished head assembly.

formats, as they are called in NASTRAN, for static and seven for dynamic analysis.

In this problem, the stress and deflection were desired. However, it is possible to save the problem solution and to restart and perform a different analysis at a later date, possibly a vibration analysis, without duplicating the original effort.

The documentation for the NASTRAN Computer Program consists of three manuals; the Theoretical Manual, the User's Manual, and the Programmer's Manual.

The Theoretical Manual is a commentary on the program. It is, first of all, intended to be an introduction to NASTRAN for all interested persons, including those who will use the program and those whose interests are less direct. For this purpose, the structure and the problem-solving capabilities of the program are described in a narrative style. The manual's most important function, however, is to justify the analytical and numerical procedures that underlie the program by presenting explanations and derivations of sufficient depth to be convincing.

The selection of material has not been an easy task because not everyone has the same concept of what the word "theory" means when it is applied to a computer program. A broad view concerning the selection of materials has been adopted; i. e., the formulation that will be solved, the development of the procedures or algorithms that will be used in the solution, the organization of the program, and the flow of data through the computer.

The User's Manual contains all of the information needed to solve problems with NASTRAN. It includes instruction in structural modeling techniques, instruction in input preparation, and information to assist the interpretation of output. It contains descriptions of all input data cards, restart procedures, and diagnostic messages.

The Programmer's Manual contains the information that is required for maintenance and modification of the program. It contains a complete description of the program code including the mathematical equations that are implemented in the Functional Models and describes the Executive System and the coding practices that have been employed.

The NASTRAN program is currently operational on the IBM 7094/7040, the IBM 360 models 50 through 95, the CDC 6400, 6500, and 6600, and the Univac 1108 Exec II computer systems. The plotters that can be utilized with these systems are the Stromberg Carlson 4020, the Benson Lehner LTE or STE, the Electronics Associates EIA 3500, the Display Data DD80, and the Calcomp 763.

Now that the initial development phase has been completed, there will be continuing maintenance by a NASTRAN Management Center at a yet undetermined NASA Center. The Office of Advanced Research and Technology will fund the maintenance and development tasks. In other words, the program will not become stagnant or die. In fact, the first year's improvements have been determined and priorities have been assigned. A few examples are:

1. Substructure Partitioning
2. Finite Element Thermal Analyzer
3. Dummy Element
4. Single Precision Option
5. Training Films

NASTRAN is the perfect tool to be used in the development of the shuttle vehicle. It will, first of all, do the job and do it efficiently; it will allow the monitoring NASA Centers, the prime contractors, the subcontractors, and other interested parties to exchange information freely and to converse in a common language; and possibly of equal importance, with the correct management and guidelines, it can save untold development time and costs.

SKYLAB DOCKING RESPONSE ANALYSIS

By

W. B. Holland

ABSTRACT

The salient features of the mathematical formulation and digital algorithm developed by Martin-Marietta Corporation, Denver Division for the Skylab docking response analysis are presented. The mathematical model considers the docking to be in proximity such that collision is imminent. The coupling of the docking mechanism and the elastic responses of the vehicles are included. The Apollo probe/drogue docking system is considered.

INTRODUCTION

The docking maneuver and its associated structural responses is a primary consideration in the design of large flexible space structures such as Skylab. The Martin-Marietta Corporation, Denver Division under contract to Marshall Space Flight Center has developed the methodology and digital

algorithm to determine the response of two elastic vehicles during the docking maneuver. The objective of this paper is to present the salient features of their analysis. More rigorous explanations and developments are contained in References 1 through 3.

Many authors have analyzed the docking maneuver in recent years. In general, their formulations were restricted to consideration of rigid vehicles. Their docking analysis was performed in two steps; (1) calculation of the force-time histories at the docking mechanism between the vehicles and (2) application of the force-time histories from step 1 to elastic response analyses of the respective bodies. This procedure is referred to as the "two-step method." It was shown in Reference 4 that the two-step method can yield very conservative elastic responses for a highly flexible structure such as Skylab (Fig. 1). More realistic responses and loads are attainable by applying a "one-step method", wherein the effects of docking elastic rather than rigid vehicles are included. The Skylab Docking Response Analysis is a one-step method.

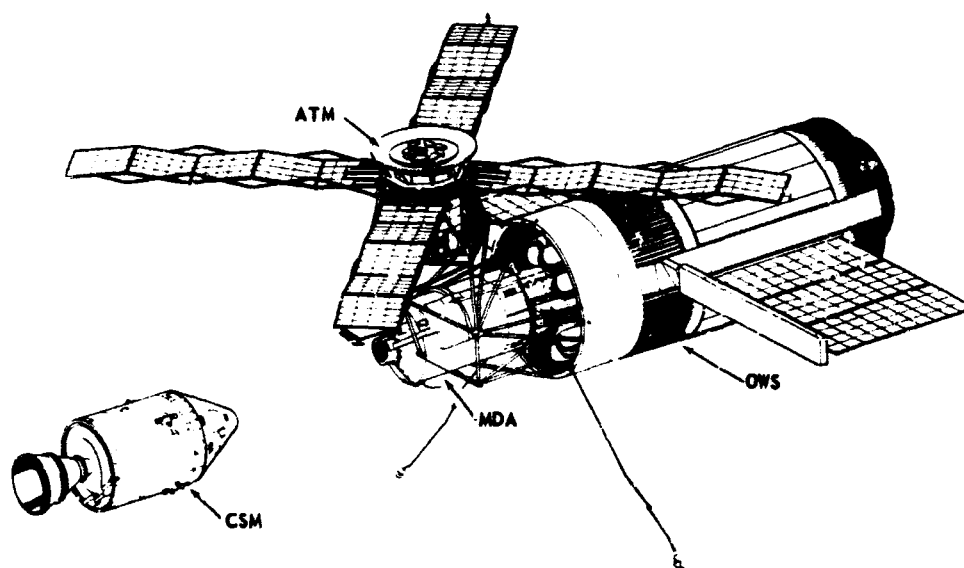


Figure 1. Skylab docking configuration.

PHYSICAL PROBLEM

The docking maneuver can be described as a controlled collision of two vehicles. The vehicles are considered to be initially in proximity such that collision is imminent. Each vehicle has a docking mechanism that serves to (1) dissipate the relative kinetic energy, (2) align the vehicles, and (3) bring the vehicles together and thus achieve a structural tie.

The Apollo probe/drogue docking system (Fig. 2) is utilized in the Skylab program. The docking probe is mounted on the command service module (CSM), and a drogue is mounted on the Skylab cluster at a radial docking port and also at the axial docking port. The CSM will be referred to as the chase vehicle, and the cluster will be referred to as the target vehicle.

The docking probe (Fig. 3) consists of a central body, probe head, pitch arms, tension links, hydraulic attenuators, capture latches, and support structure. The central body contains an inner cylinder that allows relative axial motion (10-inch stroke) with respect to an outer cylinder. The probe head is gimbal mounted on the inner cylinder and houses capture latches that engage the drogue apex.

The pitch arms and tension links act to align the vehicles and prevent any jack-knifing motion.

The attenuators are fluid-displacement type units and are the primary sources of energy dissipation. The geometry of the probe and drogue is such that the potential points of contact are the probe head on the drogue surface and the pitch arms on the drogue lip.

ANALYTICAL DEVELOPMENT

During the course of the docking simulation, there are constraints that result from the geometry of the docking mechanism. As an example, consider the requirement that the motion of the probe head be constrained to be coincident with the motion of the drogue apex when the probe head is captured. Such conditions of constraint do not exist a priori, but are maintained by strong forces. It is a distinct advantage of the Lagrangian method [5] that allows one to formulate the equations of motion for a system with constraints without knowledge of the constraint forces. The constraint forces are implied by constraint equations. Now, the form of Lagrange's equations with auxiliary conditions of constraint are cited.

EQUATIONS OF MOTION

Consider the dynamical system to be characterized by discrete coordinates

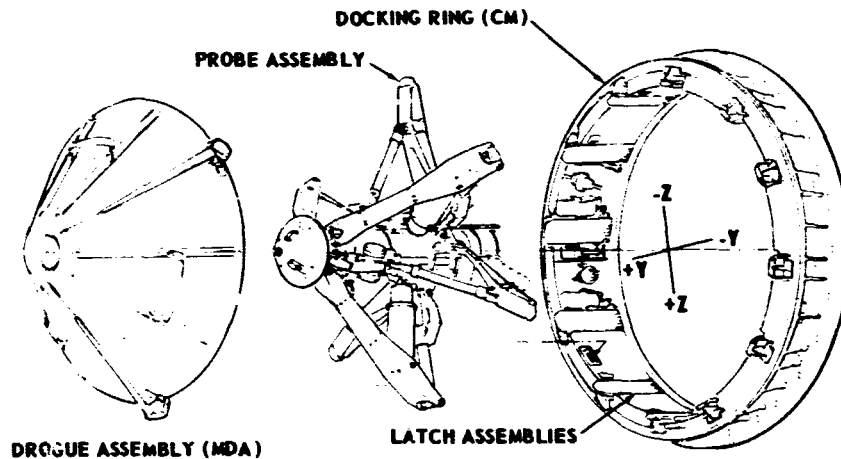


Figure 2. Docking system major assemblies.

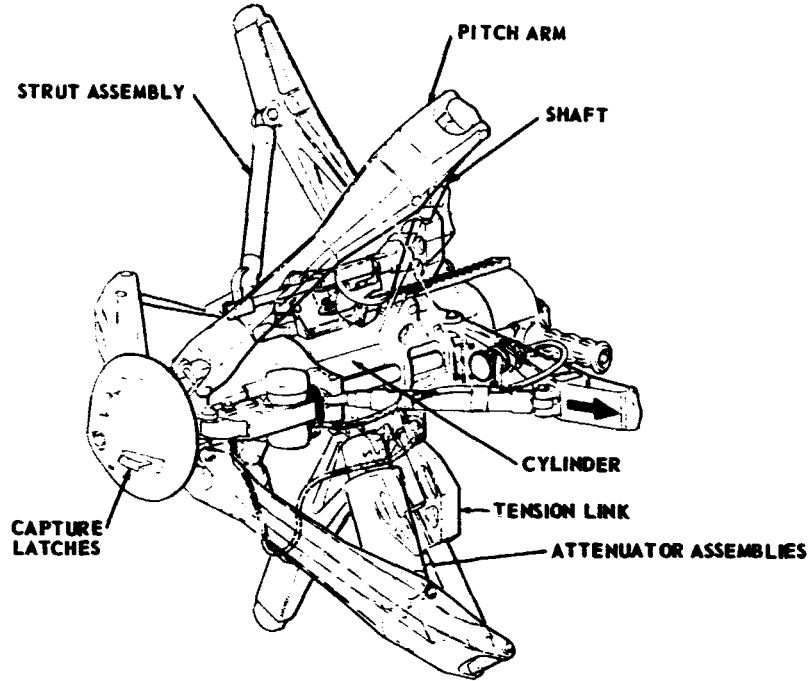


Figure 3. Probe docking system.

$$q_1, q_2, \dots, q_n \quad (1)$$

The motion of the coordinates is restricted by kinematical conditions. These auxiliary conditions of constraint may be expressed in general form as

$$\bar{\phi}_s = \bar{\phi}_s(q_1, q_2, q_n, \dot{q}_1, \dot{q}_2, \dot{q}_n; t, dt) = 0 \quad (2)$$

$$s = 1, 2, \dots, m$$

The Lagrange equations of motion can be expressed as

$$\frac{d}{dt} \left(\frac{\partial T}{\partial \dot{q}_k} \right) - \frac{\partial T}{\partial q_k} = Q'_k + \sum_{s=1}^m \bar{\lambda}_s \cdot \phi_s \quad (3)$$

In the above equation, T is the kinetic energy of the whole system. The generalized forces, Q'_k , are associated with all impressed forces both conservative and nonconservative. The Lagrangian multiplier, $\bar{\lambda}_s$, is a measure of the microscopic violation of the constraint equation $\phi_s = 0$, and is equivalent to the

forces required to maintain the constraint. The m equations of constraint coupled with the n differential equations of motion are sufficient to solve for the n unknowns, q_n ; and for the m unknowns, $\bar{\lambda}_m$.

In general, it is more convenient to apply equations (2) and (3) in matrix form. To achieve a matrix form, consider a transformation matrix, $[\beta]$, where

$$\{u\} = [\beta]\{\dot{q}\} \quad (4)$$

The vector $\{u\}$ contains nonholonomic velocities (velocity components projected on a totaling coordinate system).

A matrix $[P]$ is defined such that the k th row of $[P]$ is

$$(k\text{th row of } [P]) = \{\dot{q}\}^T \left[\frac{\partial \beta}{\partial q_k} \right]^T \quad (5)$$

The auxiliary conditions of constraint (equation 2) are expressed in the form

$$\bar{\phi}_s = \sum_{k=1}^n \bar{b}_{sk} \dot{q}_k + \bar{\phi}_{st} = \bar{0} \quad (6)$$

The term $\bar{\phi}_{st}$ has been added to account for rheonomic constraints. The kinetic energy, T , may be expressed in terms of the nonholonomic velocities and a mass matrix $[M]$, or

$$T = \frac{1}{2} \{u\}^T [M] \{u\} \quad (7)$$

With equations (4 through 7), equations (2) and (3) can now be written in matrix form as

$$\begin{aligned} [\beta]^T [M] \{\dot{u}\} + ([\beta]^T - [P]) [M] \{u\} \\ = \{Q^*\} + [b]^T \{\lambda\} \end{aligned} \quad (8)$$

and

$$[b] \{\dot{q}\} + \{\phi_t\} = \{0\} \quad (9)$$

The matrix $[\beta]$ is a square matrix that is, in general, non-singular; then,

$$\{\dot{q}\} = [\beta]^{-1} \{u\} \quad (10)$$

Now, if equation (8) is pre-multiplied by $([\beta]^T)^{-1}$ and equation (10) is substituted into equation (9), the following is obtained

$$\begin{aligned} [M] \{\dot{u}\} + ([\beta]^T)^{-1} ([\beta]^T - [P]) [M] \{u\} \\ = ([\beta]^T)^{-1} (\{Q^*\} + [b]^T \{\lambda\}) \end{aligned} \quad (11)$$

and

$$[b] [\beta]^{-1} \{u\} + \{\phi_t\} = \{0\} \quad (12)$$

Equation (11) represents n differential equations of motion and equation (12) represents the m equations of constraint. The derivation of the explicit forms of the matrices $[P]$, $[\beta]$, and $[b]$ are too lengthy to include here and can be found in Reference 2.

STATE VECTOR

The equations of motion and auxiliary equations that characterize the docking maneuver comprise

a set of first order differential equations of the general form

$$\dot{Y}_i = f_i(Y_1, Y_2, \dots, Y_n, t) \quad (13)$$

where

$$i = 1, 2, \dots, n$$

The elements of the vector $\{Y\}$ completely define the state of the system at any time. The relationships between $\{Y\}$, $\{\dot{Y}\}$, and t are the equations of motion, constraint, and auxiliary equations that describe the behavior of the system. The elements of $\{Y\}$ are initially given; by evaluating $\{\dot{Y}\}$ numerically, inputs into an integration algorithm that serves to increment $\{Y\}$ are obtained.

Let us define the elements of the state vector $\{Y\}$.

$$\{Y\} = \begin{bmatrix} \{u_T\} \\ \{X_T\} \\ \{\gamma_T\} \\ \{u_C\} \\ \{X_C\} \\ \{\gamma_C\} \\ \{\rho\} \\ \{\xi_T\} \\ \{\xi_T\} \\ \{\xi_C\} \\ \{\xi_C\} \\ \{\delta_{Cs}\} \end{bmatrix}, \quad (14)$$

where

$$\{Y_T\} = \begin{bmatrix} u_T \\ v_T \\ w_T \\ \omega_{xT} \\ \omega_{yT} \\ \omega_{zT} \end{bmatrix}, \quad (15)$$

$$\{X_T\} = \begin{bmatrix} X_T \\ Y_T \\ Z_T \end{bmatrix}, \quad (16)$$

and

$$\{\gamma_T\} = \begin{bmatrix} \gamma_{11T} \\ \gamma_{12T} \\ \gamma_{13T} \\ \gamma_{21T} \\ \gamma_{22T} \\ \gamma_{23T} \end{bmatrix} \quad (17)$$

The parameters u_T , v_T , and w_T are components of translational velocity of the target vehicle's center of mass, referred to the target body-fixed system (Fig. 4). The components of angular velocity of the target body-fixed system are ω_{xT} , ω_{yT} , and ω_{zT} . The vector positioning the target vehicle's center of

mass from the origin of the inertial frame and referred to the inertial frame has components X_T , Y_T , and Z_T . The orientation of the target vehicle's body axes with respect to the inertial system is given by the six direction cosines, γ_{ijT} . The vectors $\{u_C\}$, $\{x_C\}$, and $\{\gamma_C\}$ have corresponding definitions for the chase vehicle. The vector $\{\rho\}$ contains six parameters that describe the state of the probe assembly,

$$\{\rho\} = \begin{bmatrix} \rho_x \\ \alpha_y \\ \alpha_z \\ \gamma_1 \\ \gamma_2 \\ \gamma_3 \end{bmatrix} \quad (18)$$

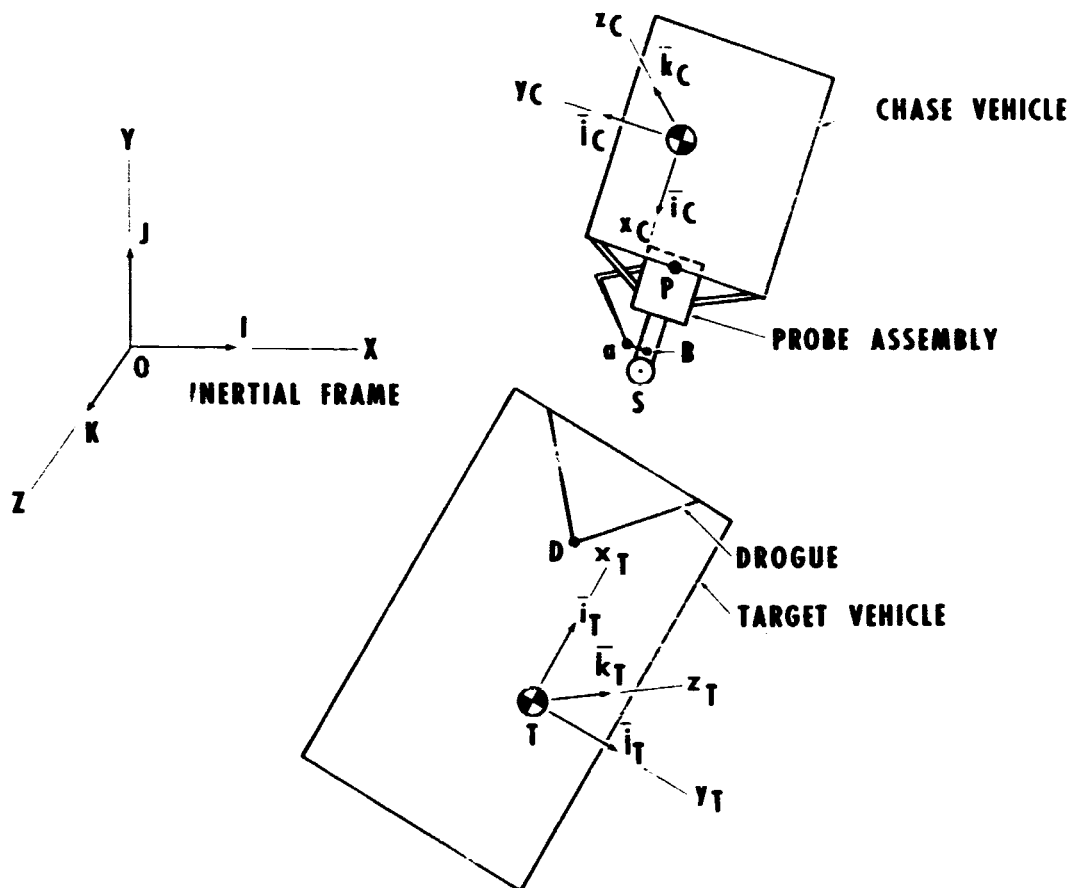


Figure 4. Coordinate systems.

The coordinate ρ_x describes the extension of the inner cylinder (Fig. 5). The angular deformation of the probe body resulting from elastic deflections of the probe support struts is described by the coordinates γ_y and γ_z . The coordinates ($\gamma_1 = 1, 2, 3$) are the angles included between the pitch arms and the probe central body.

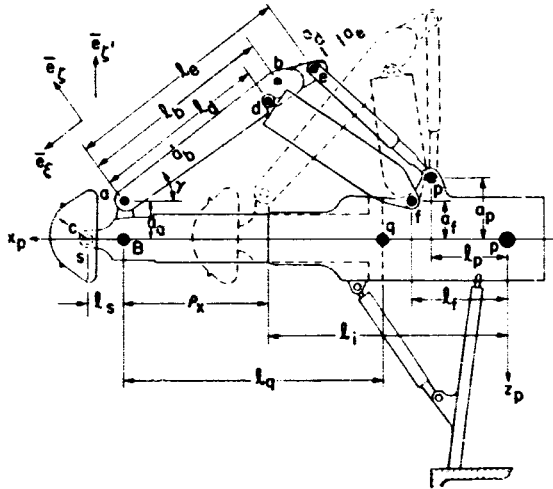


Figure 5. Probe mechanism geometry.

The elastic deflections of the target and chase vehicles are expressed as a superposition of normal free-free elastic modes of the respective vehicles. The vectors $\{\xi_T\}$, $\{\xi_C\}$ contain the normal coordinates of the elastic modes of the target and chase vehicles, respectively. The vector $\{\delta_{Cs}\}$ contains the attitude control system parameters that are required to close the loop.

CONSTRAINT CRITERIA

There is a variety of combinations of constraint conditions that are to be implemented during the course of a motion simulation. The constraint criteria permit the mathematical model to simulate the various events that occur during the maneuvering in a representative manner. The motion during the maneuver is characterized by the bumping, sliding, breaking contact, and capture of the docking mechanisms.

A parameter ϕ_i is associated with each of the constraint conditions. The constraints are identified in Table 1.

TABLE 1. DESCRIPTION OF THE CONSTRAINTS [1]

| Constraint Parameter | Description |
|-------------------------------|---|
| $\phi_j, j = 1, 2, 3$ | jth Tension Link Constraint $\phi_j = pe _0 - pe _j; \phi_j \geq 0.$ |
| ϕ_4 | Probe Head Contact Constraint $\phi_4 = -DS \cdot \frac{e}{\alpha} - C; \phi_4 \geq 0.$ |
| ϕ_{j+4} $j = 1, 2, 3$ | jth Pitch Arm Contact Constraint $\phi_{j+4} = \overline{QR}_j \cdot \overline{m}_j - A_b; \phi_{j+4} \geq 0$ |
| ϕ_8 | Probe Head Capture Constraint $\phi_8 = DS - C/\sin \alpha; \phi_8 \geq 0$ |

Because of the nature of the docking system, there are certain constraints that cannot physically occur at the same time. For example, the j th tension link cannot be in tension when the j th pitch arm is in contact with the drogue lip; i. e., ϕ_j and ϕ_{j+4} cannot simultaneously be equal to zero. A similar conflict exists between ϕ_4 and ϕ_8 . This means that during the motion, if $\phi_i = 0$, then the corresponding constraint equation is a candidate to be used. When a conflict in constraint conditions occurs, the dominant condition is chosen.

There is a constraint force, λ , corresponding to each of the constraint equations. If a particular constraint equation is not in effect, its corresponding constraint force is zero. When particular constraint equations are in effect, the certain elements of the $\{\dot{Y}\}$ vector are solved to satisfy the constraint equations. The subvector $\{\dot{\rho}\}$ is that portion of $\{\dot{Y}\}$ that is committed to satisfy the constraint equations.

NUMERICAL EXAMPLE

A docking response analysis was accomplished considering the CSM docking to the axial port of the

cluster. The elastic modes of the cluster were included in one case and omitted in another. The CSM was considered rigid (inelastic) in both cases. For a given set of initial conditions, the docking force time histories were calculated and are plotted

in Figures 6 and 7. The docking force is the resolution of the constraint forces to point D (Fig. 4). It is noted that the maximum force resulting from the elastic simulation is significantly less than that from the inelastic simulation.

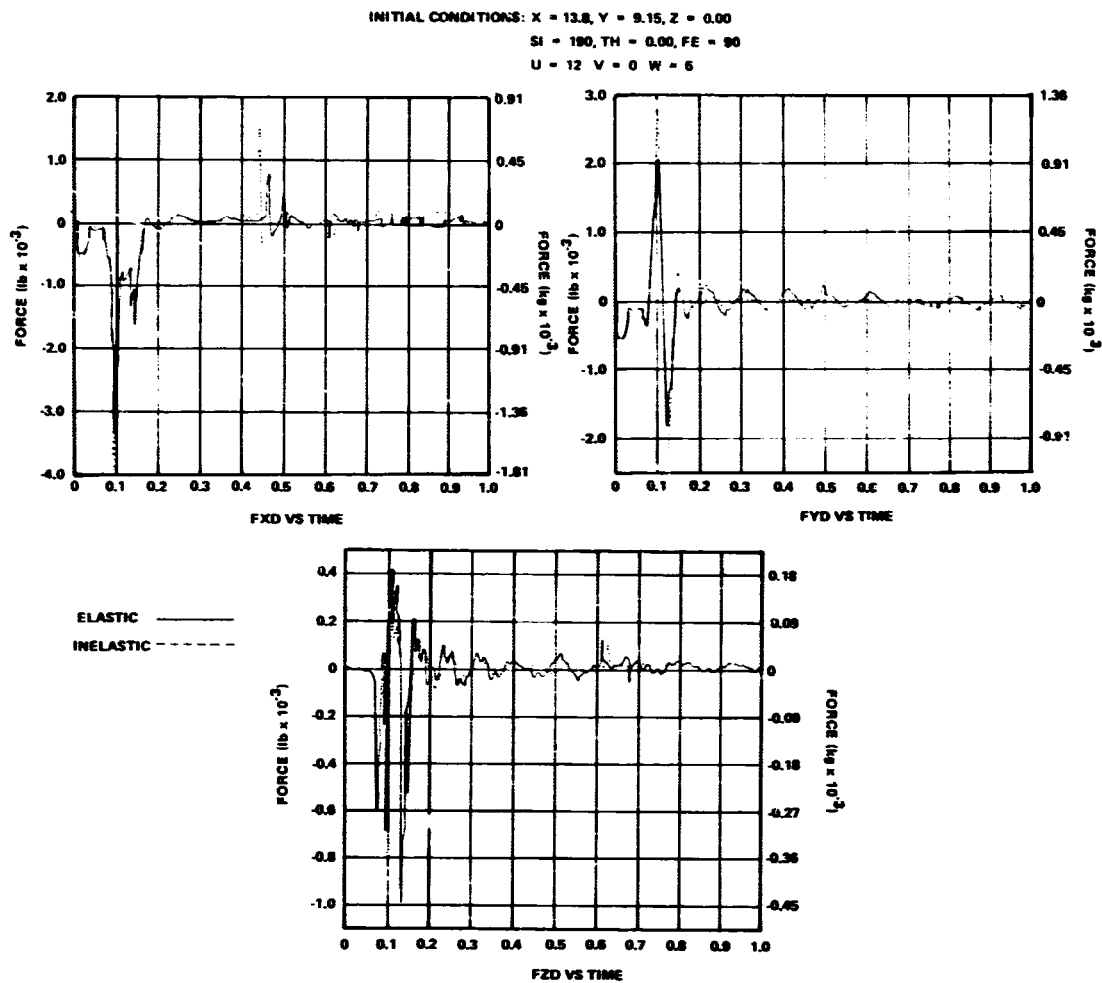


Figure 6. Docking force time history.

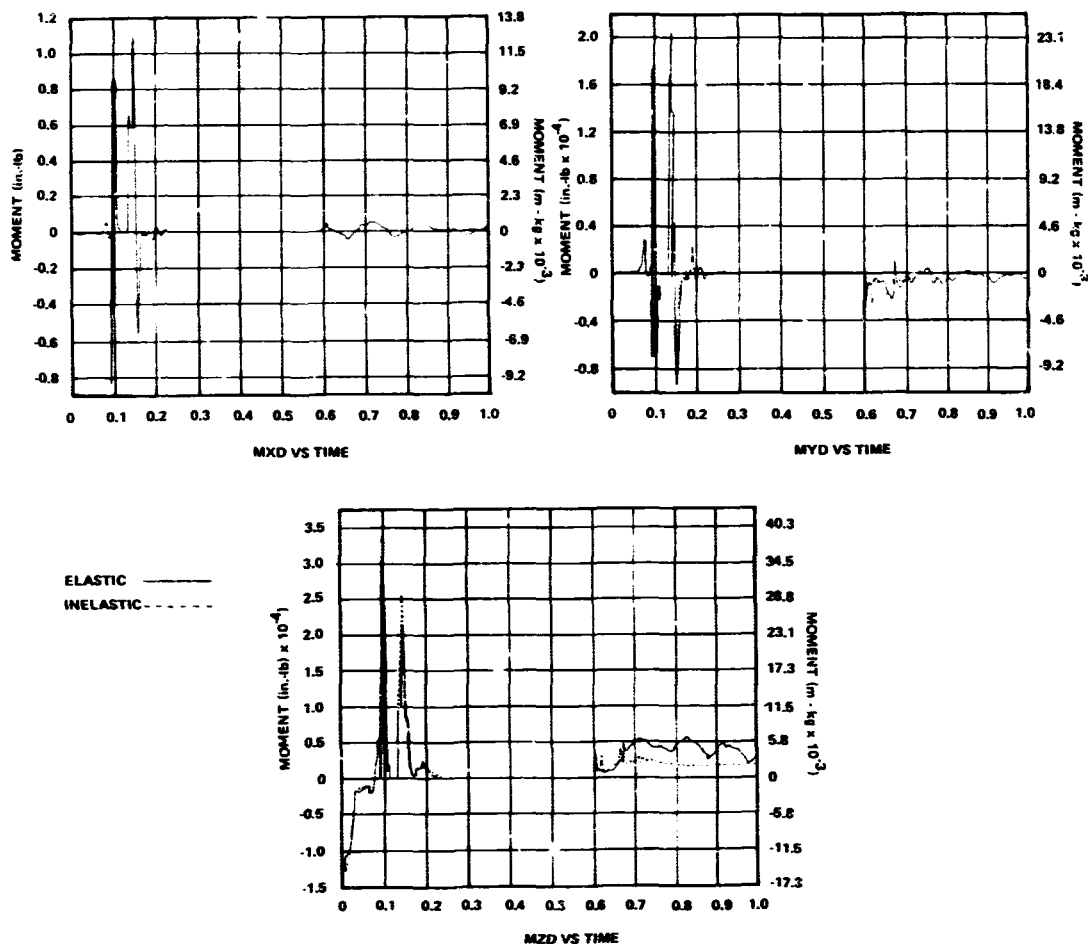


Figure 7. Docking force time history.

REFERENCES

1. Bodley, C. S.; and Park, A. C.: Docking Probe Analytical Model. Report no. ED-2002-770, April 6, 1970.
2. Bodley, C. S.; and Park, A. C.: Response of Flexible Space Vehicles to Docking Impact. Contract NAS8-21280, March 1970.
3. Bodley, C. S.; Holland, W.; and Morosow, G.: A Method for Digital Computation of Spacecraft Response in the Docking Maneuver. Proceedings AIAA Structural Dynamics and Aeroelasticity Specialist Conference, April, 1969.
4. Hough, W. W.: Structural Loads Induced by AAP Spacecraft Docking Dynamics. Case 620, Bellcomm Report, April, 1968.
5. Lanczos, C.: The Variational Principles of Mechanics. Chapter V, University of Toronto Press, Toronto, 1964.

PAYLOAD ENCLOSURE NOISE REDUCTION

By

B. E. Erwin

INTRODUCTION

During launch, aerospace structures are subjected to very high acoustic pressures on the exterior surface of the vehicle. These pressures cause the relatively thin skinned panels and shell components of the structure to vibrate. Vibration of the exterior skin generates internal noise fields that in turn act as fluctuating pressure sources for internal equipment. Internal systems such as payloads within the upper stages of the launch vehicle are extremely sensitive to these fluctuating pressures. These payloads are enclosed by cylindrical and conical shells, which are called payload enclosures. To minimize payload vibrations, it is necessary to maximize the noise reduction through the enclosure structure.

DEFINITION OF PROBLEM

Noise reduction became a severe problem during design of the payload enclosure for the Skylab. When the Skylab program originated, the honeycomb Spacecraft Lem Adapter (SLA) was selected as the enclosure structure since it was developed hardware being utilized on the Apollo vehicle configurations. However, there arose several structural problems associated with the SLA that involved payload interference, separation constraints, and a payload weight margin. To alleviate these problems, a skin-stringer enclosure was designed by MSFC. A sketch of these enclosures is shown in Figure 1. The SLA enclosure was 4.3-cm (1.7 in.) thick honeycomb, 11.89 m (39 ft) in height, and 6.61 m (21.7 ft) in diameter. The skin-stringer enclosure was 12.5 m (41 ft) in height and also 6.61 m in diameter. The skin thickness was 0.10 cm (0.04 in) and the stringer spacing was 17.8 cm (7 in.). A comparison of the noise reduction capabilities of these enclosures is presented in Figure 2.

The SLA provided 5 to 10 dB more noise reduction across the frequency spectrum. It should be pointed out that most of the payload components and subsystems had been bought and/or tested to vibroacoustic levels

based on the SLA noise reduction. Therefore, if the skin-stringer enclosure was to be used, its noise reduction capability must be increased to yield approximately the same internal acoustic levels as the SLA.

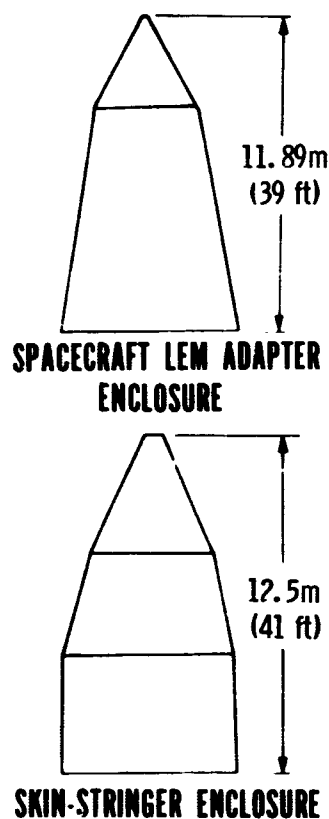


Figure 1. Skylab enclosure designs (Saturn IB wet workshop).

PROPOSED SOLUTION

Several techniques were considered for increasing the noise reduction of the skin-stringer enclosure. They are as follows:

1. Increase enclosure mass and stiffness to reduce enclosure vibration levels.

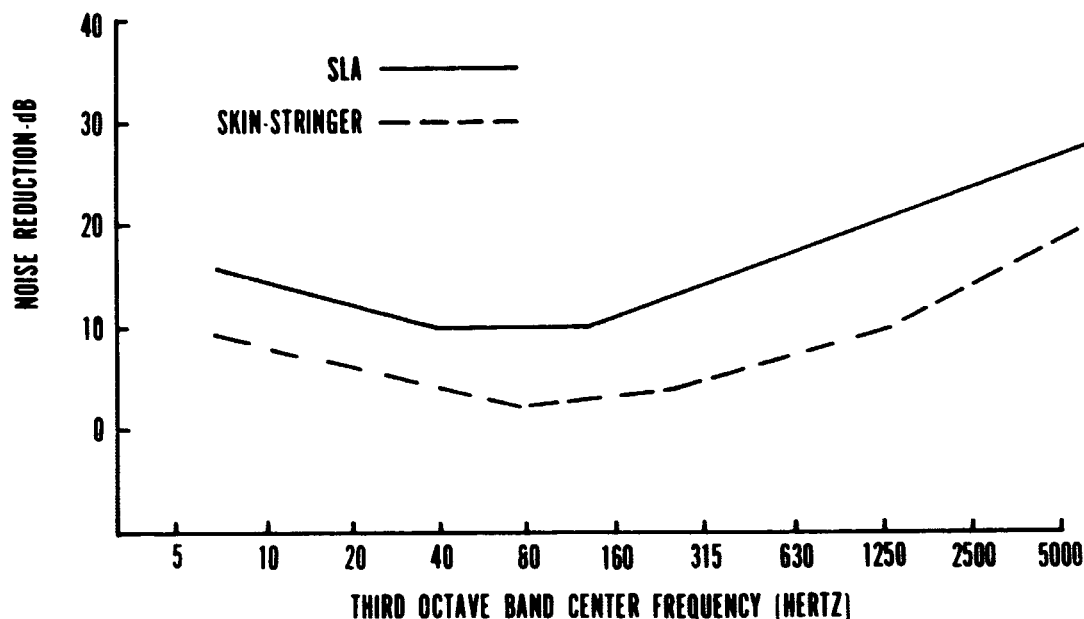


Figure 2. Comparison of noise reduction for SLA and skin-stringer enclosure.

2. Add absorption material to the internal surface of the enclosure to reduce the internal sound field.

3. Employ a light inert gaseous medium, such as helium, internal to the enclosure to provide an impedance mismatch between the air (external) and the helium (internal).

The first of these techniques was eliminated because of the payload weight restriction. The addition of an absorptive material and the utilization of the helium gas were selected for further investigation.

Helium was selected since it is the lightest, non-flammable gas available and therefore provides maximum noise reduction through a maximum impedance mismatch. The impedance of an unbounded acoustic medium is a function of ρC (the mass density times the speed of sound in the medium). The term ρC can be thought of in terms of momentum density. Since C is the speed of sound in the medium or the speed at which mechanical energy propagates in the medium, ρC may be regarded as the momentum per unit volume that may propagate through the medium. If a system is composed of two media having different values of ρC , an impedance mismatch occurs at the

interface and the inefficiency of the system is increased. That is, the medium with the smaller value of ρC is capable of absorbing and transmitting a smaller amount of momentum than the medium with a greater value of ρC . The excess momentum remains in the medium of greater ρC in the form of a reflected wave [1]. The ratio of the impedance (ρC) of helium to air is approximately 0.407, and since the sound pressure level varies proportionally with the impedance, the expected noise reduction was predicted as follows:

$$N.R. = 20 \log \frac{\rho C_{He}}{\rho C_{Air}} = 8 \text{ dB}$$

A survey indicated that accomplishing noise reduction in this manner was without precedent and would require careful laboratory testing.

TEST PROCEDURE

An applied research test program was formulated to evaluate and verify the noise reduction capability of the helium and absorptive material. A series of acoustic tests was conducted in the MSFC acoustic research facility utilizing a monocoque stainless steel

cylinder 91.44 cm (36 in.) in diameter, 91.44 cm (36 in.) long, and 0.046 cm (0.018 in.) thick and capped at both ends. A typical test setup is presented in Figure 3. The test specimen was suspended from the ceiling of the reverberation room by bungee cords and was subjected to broadband random acoustic excitation [2].

Five microphones were distributed external to the cylinder, and five microphones were distributed internal to the cylinder. The helium purge inlet and

outlet flow attachments were installed in the bottom cap. Samples taken from the bottom of the cylinder indicated a helium purity of at least 93 percent for each test run. The tests were conducted for the following configurations:

1. Unmodified cylinder with ambient air inside the cylinder.
2. Unmodified cylinder with the internal volume purged with helium.

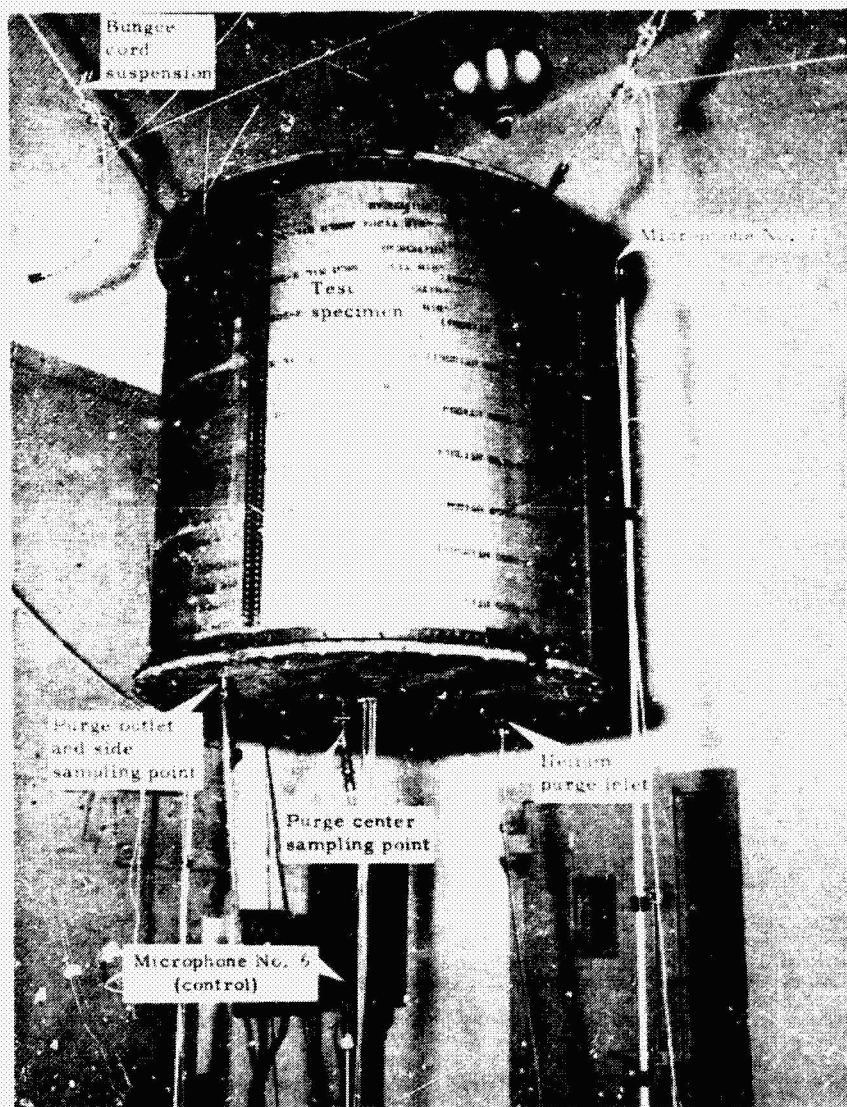


Figure 3. Typical test setup.

3. Cylinder modified with 2.54-cm (1-in.) thick polyurethane foam applied to all interior surfaces and ambient air inside the cylinder.

4. Cylinder modified with 2.54-cm (1-in.) thick polyurethane foam applied to all interior surfaces and the internal volume purged with helium.

DATA REDUCTION

Data from the microphones were recorded on magnetic tape. One-third octave band analyses were subsequently performed on the recorded data. The data were plotted in decibels at one-third octave band center frequencies. To obtain an estimate of noise reduction for the cylinder, the average internal microphone levels were subtracted from the average external levels, and the resulting noise reduction

curves were plotted. This is the form in which the results are presented in this paper.

TEST RESULTS

The results from these tests show that the use of helium was quite effective in providing additional noise reduction. These effects are shown in Figure 4 by comparing the noise reduction measured when the cylinder was filled with helium and when filled with air. The air volume critical frequency at 182 Hz and the helium volume critical frequency at 530 Hz are volume resonance phenomena that are a function of the media. These resonances, as expected, are indicated by a decrease in the measured noise reduction. A significant decrease in noise reduction also occurred near the ring frequency, which was calculated to be approximately 1800 Hz. It is a

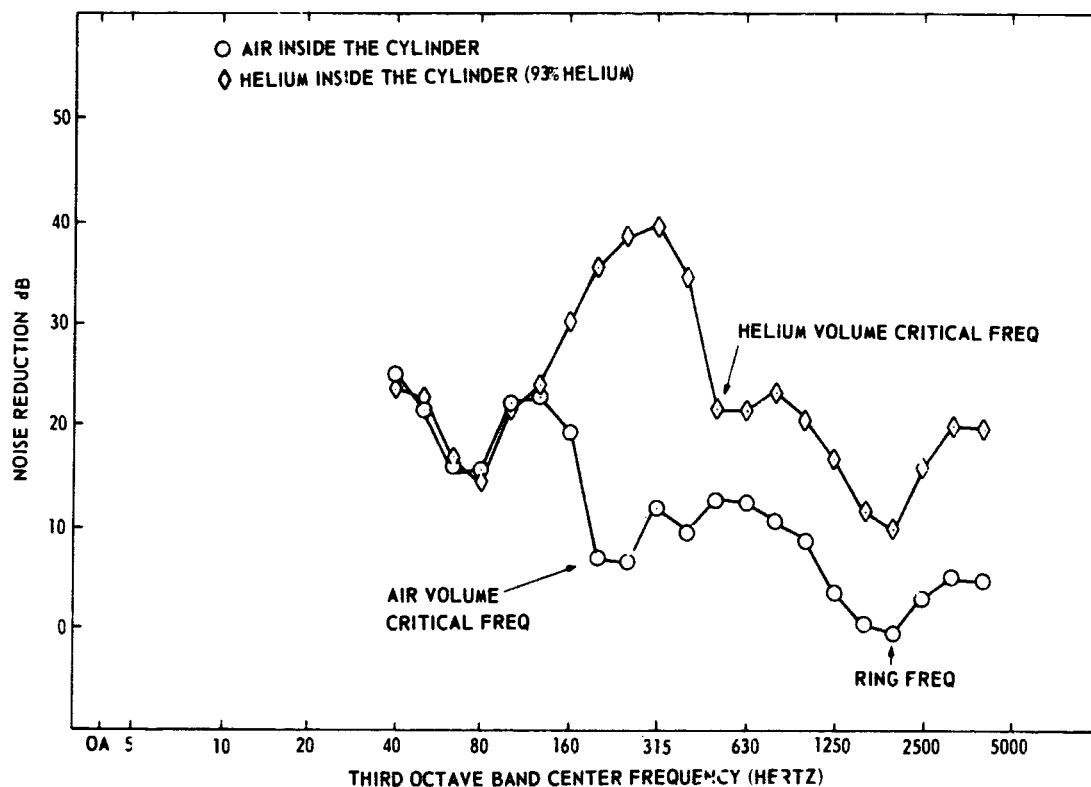


Figure 4. Noise reduction of a monocoque cylinder in a reverberant acoustic field.

well-known property of cylindrical structures that response is highest at the ring frequency, thus causing another decrease in noise reduction for both media. A large noise reduction was obtained in the frequency range between the air and helium volume critical frequencies. Above the helium volume critical frequency, approximately 8 to 10 dB additional noise reduction was obtained. In scaling from the test cylinder to the 6.61-m (21.7-ft) diameter payload enclosure, the air and helium volume critical frequencies would shift down in frequency to 25 Hz and 70 Hz, respectively. Thus, it can be assumed that the helium will provide 8 to 10 dB added noise reduction for the payload enclosure in the frequency spectrum above 25 Hz.

The noise reduction furnished by the absorptive material was frequency-dependent as shown in Figure 5. In the frequency band from 40 to 100 Hz, the absorptive material provided practically no noise reduction above that afforded by the cylinder.

However, from 600 to 3000 Hz, reductions of 2 to 6 dB in sound pressure levels were obtained. An unexpected result was the magnitude of added noise reduction indicated from 100 to 600 Hz. This effect was attributed to the added mass and stiffness caused by the presence of the foam since the cylinder was monocoque and only 0.046 cm (0.018 in.) thick.

Another series of tests was run with the cylinder modified with the 2.54-cm (1-in.) layer of foam and purged with helium. These results, presented in Figure 6, show that the foam and helium furnished approximately 25 dB in the frequency range above the helium volume critical frequency. These results indicate a greater noise reduction than the added results of the helium and absorptive test taken separately. This observation implies that the absorption material was more efficient in the helium environment. However, no theoretical basis was found to support this observation.

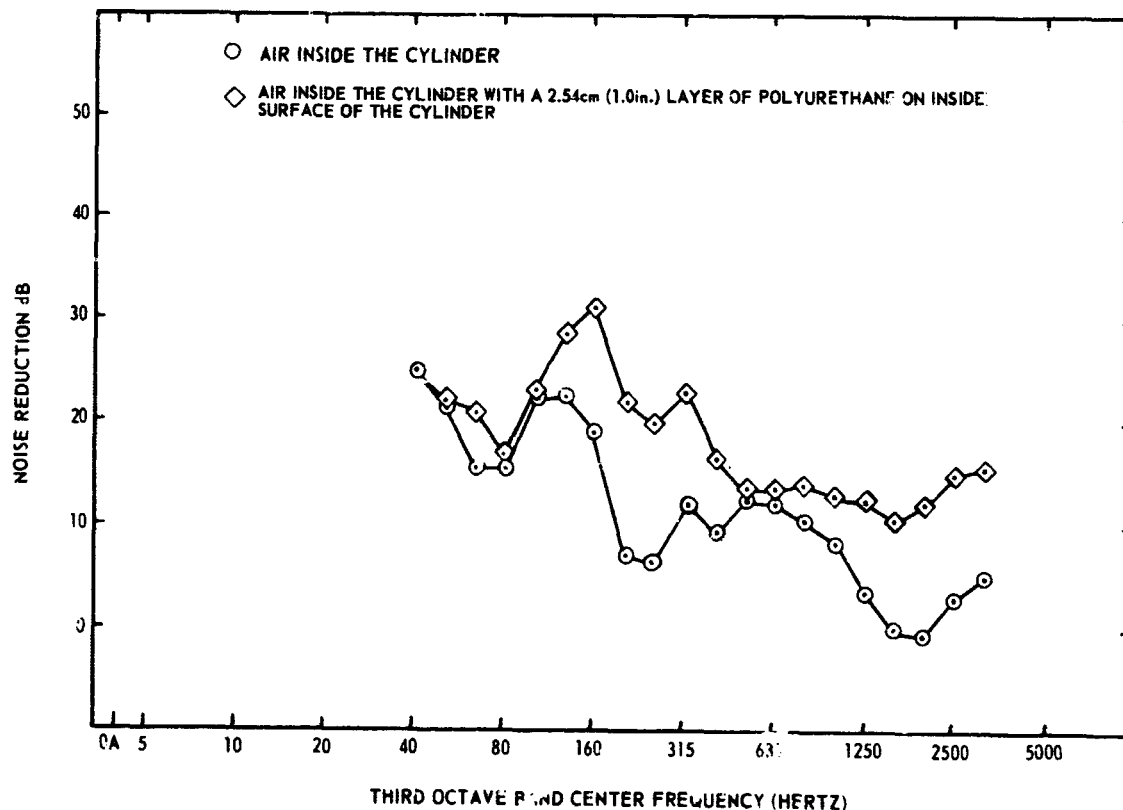


Figure 5. Noise reduction of a monocoque cylinder in a reverberant acoustic field.

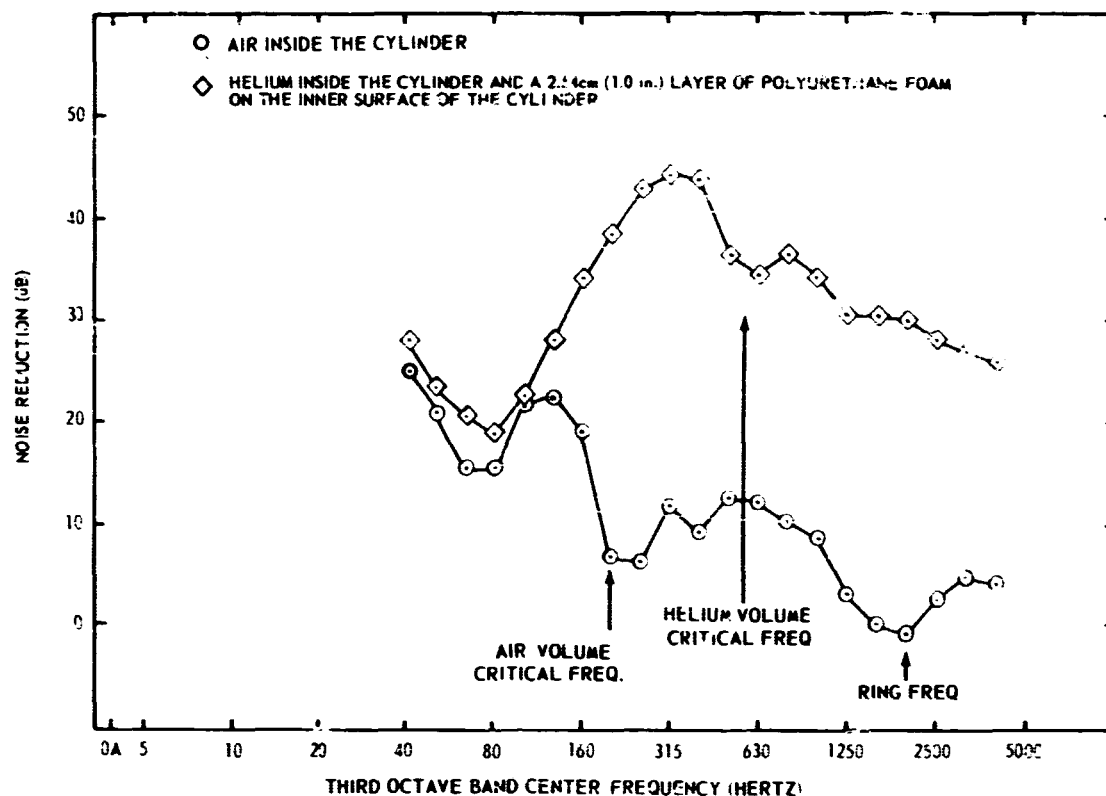


Figure 6. Noise reduction of a monocoque cylinder in a reverberant acoustic field.

CONCLUSIONS

An added noise reduction of 8 to 10 dB can be obtained for a cylindrical structure with an internal helium environment. The noise reduction provided by polyurethane foam absorptive material is frequency-dependent. Reductions of 2 to 5 dB were obtained in the frequency region of 600 to 3000 Hz. The conclusions from the helium test were the basis for an operational requirement to purge the payload enclosure with helium prior to launch. This requirement specified that a 93-percent helium environment be maintained up to 15 sec after launch.

Since the research effort reported in this paper, several additional acoustic tests have been performed to investigate the effect of a helium purge on component vibration response. A portion of these tests were sponsored under research contract NAS8-20260 with Wyle Laboratories. Another series of tests involved a large 6.71 m (22-ft) diameter cylinder mounted on the Mobile Acoustic Research Lab (MARL) test fixture located at the Mississippi Test Facility. The MARL was located near the test stands and exposed to four, stage-static-test exposures. During these exposures, the large cylinder was purged with helium. The results from these tests will be reported in the near future.

REFERENCES

1. Holmes, J. R.: Air-Helium Noise Reduction Studies. Wyle Laboratory, Research Staff Report WR70-3, January 1970.
2. Saunders, J. M.; and Cahill, J. B.: Acoustic Evaluation of Polyurethane Foam Lining and Helium Purging of AAP Payload Shroud. Summary Test Report, ASD-ASTN-1093, February 1970.

S-II STAGE VIBRATION TESTING AND ANALYSIS FOR THE POGO PHENOMENA

By

H. M. Lee

SUMMARY

The Dynamics Analysis Branch of the Astronautics Laboratory of Marshall Space Flight Center conducted an investigation of the longitudinal oscillation problem encountered during second stage burn of the Saturn V vehicle. This report describes the structural test and math modeling effort that was undertaken. It includes details of the extensive experimental research program performed on the S-II stage vehicle in conjunction with a definitive math model development utilizing the test information.

The tests were conducted using a shortened S-II stage to determine dynamic characteristics of the thrust structure/center engine crossbeam/liquid hydroelastic system. These data were used as direct input in developing the math model. Comparisons between results obtained from the empirical model and tests are made; these show excellent correlation in frequency, response, and mass characteristics. Also, comparisons between flight data and the calculated overall vehicle modal parameters are made to further verify the adequacy of the structural model.

INTRODUCTION

Development of large space vehicles involves the assemblage of vast amounts of hardware. Structural convergence of these components, in most cases, produces an operational system with many dynamically complex characteristics. The inflight dynamic response of these vehicles is dependent on parameters related to structural design, fluid mechanics, propulsion mechanisms, and control systems. To properly analyze dynamic problems that occur during flight, all of these effects must be taken into account.

On December 21, 1968, the first manned Saturn V vehicle (AS-503) was launched. Second stage longitudinal oscillation problems, known as POGO were first recorded during this flight. The

severity of this problem did not become apparent, however, until the flight of AS-504 (Apollo 9 mission) on March 3, 1970. Figure 1 shows recorded accelerometer response in G's versus flight time for three areas in the aft end of the S-II stage. These data were taken from oscillograms of the AS-504 lox sump, center engine, and outboard engine during S-II stage burn.

An analysis of this flight data and some previous test data revealed that the center engine crossbeam responded at a frequency near 18 Hz throughout flight. The response of the beam was of low amplitude until near the end of second stage burn. At this time the system became unstable, and the large amplitude oscillations shown in Figure 1 were encountered. It was hypothesized that one of the predominant lox bulkhead modes increased in frequency with decreasing liquid level and coupled with the crossbeam resonance to cause this instability. This would apparently indicate that as the lox bulkhead frequency approached the 18 Hz region, the total system would enter into a closed loop, regenerative mode, producing high response levels in the aft section of the S-II stage.

Because of the impact and complexity of the problem, an extensive experimental program was initiated. Figure 2 exhibits a flow chart outline of the total S-II oscillation program. This paper presents, however, only a summary of the testing, modeling techniques, and data comparisons utilized in updating, assessing, and verifying the structural model.

DESCRIPTION OF TESTS

Dynamic testing of the S-II stage was composed of three phases. Figure 3 shows the structural differences between the three phases as well as the method of dynamic excitation. The approximate location of the accelerometer instrumentation is also shown for each case. It should be noted that for phase I testing, the aft skirt was fixed to ground, but during phase II and III testing the structure was

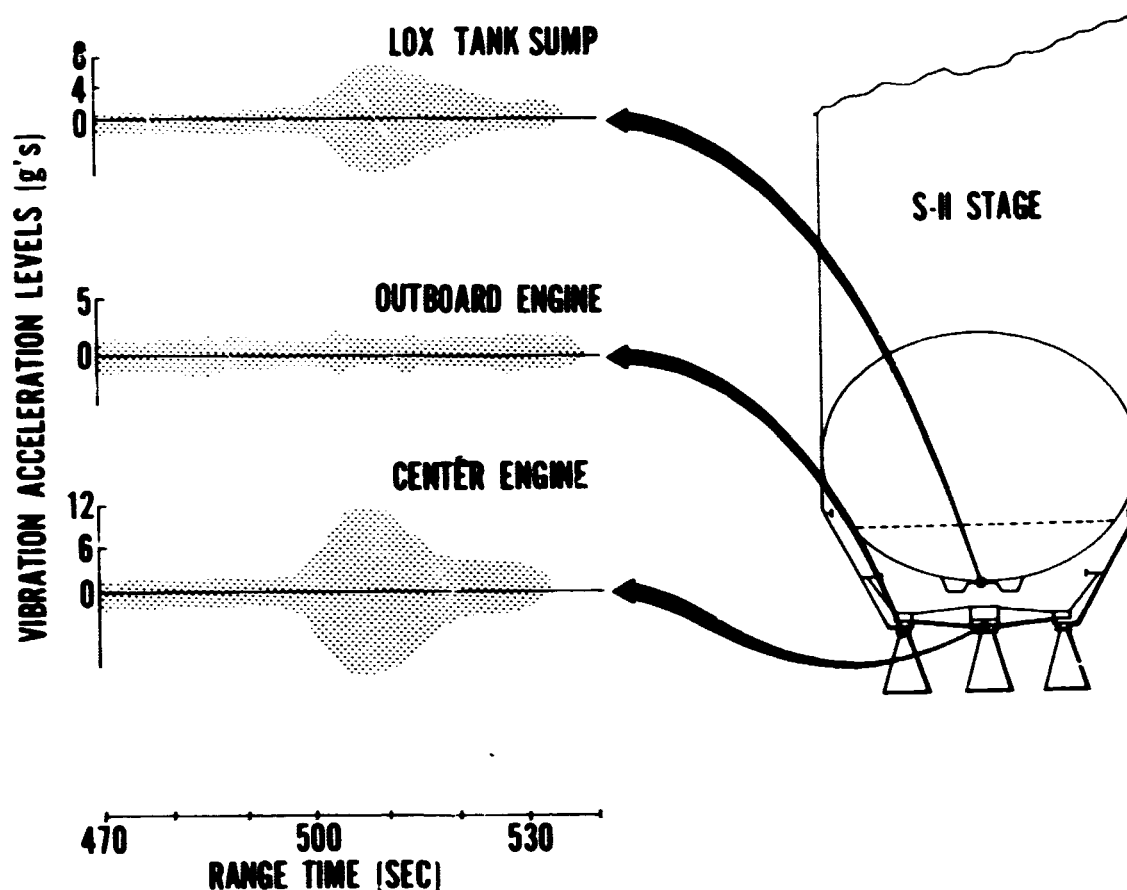


Figure 1. AS-504 vibration amplitudes.

supported on a low frequency air suspension system. The lox tank was filled with de-ionized water and drained in several incremental levels. Modal surveys, which include sinusoidal sweeps from 5 to 50 Hz and resonant frequency dwell tests, were then performed at each of the levels.

The primary objective of the phase I sequence was to empirically investigate the axisymmetric modes of the aft lox tank bulkhead as a function of propellant level, corresponding to levels prior to and through the period of longitudinal oscillation observed during the AS-504 flight. The investigation included the acquisition of such dynamic parameters as mode shapes, damping frequency, generalized mass, and tank bottom pressures. The phase II and phase III test efforts were designed to determine bulkhead/thrust structure/crossbeam modal interaction. Phase III also included the installation of the five lox

feedlines capped and filled with water. The goal of these two phases was to determine the following properties: (1) predominant system mode shapes, (2) system damping, (3) modal frequencies, (4) generalized mass, (5) effects of the lox feedlines, and (6) tank bottom/lox line pressures.

The phase I test proved to be an excellent setup for determining the axisymmetric hydroelastic modes of the lox tank bulkhead. Accelerometers were placed along several meridians over a 180-degree section of the bulkhead. Response data obtained at the same level on each meridian were then averaged to yield mode shapes. Figure 4 shows the first three bulkhead resonant frequencies versus flight time as related to the AS-504 vehicle S-II stage burn.

Phase II and III data were obtained from the structural interaction of the lox tank bulkhead, aft

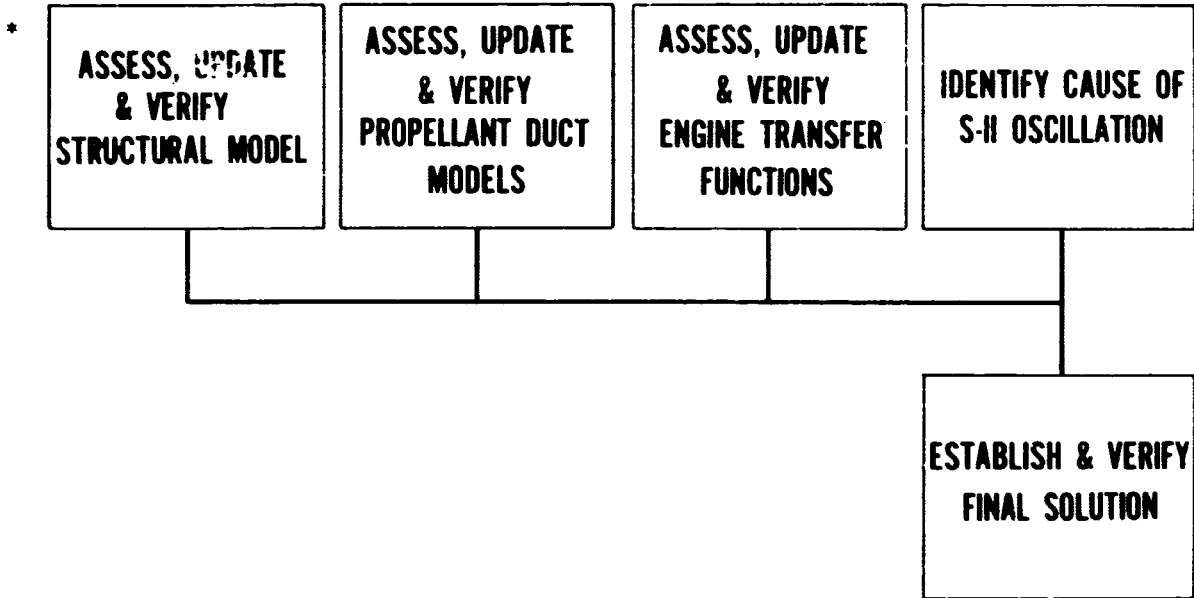


Figure 2. S-II oscillation overall program flow.

skirt, thrust structure, center engine crossbeam, and several other components. Presented in Figure 5 are the first five longitudinal S-II system modal frequencies versus AS-504 second stage flight time. Interesting modal frequency patterns can be noted in the figure because of the complex interaction of the structural components. These frequency versus time plots represent only one of the many types of forced response information obtained from the S-II testing program. It was from the data that the math model of the aft end of the S-II vehicle was defined.

MATH MODELING TECHNIQUE

A multi-degree-of-freedom model of the phase I test configuration was developed to simulate the response of the structure/fluid system. The modeling technique used is given in Reference 1. The structure and fluid were assumed to be a damped structural system subjected to harmonic forced motion. Test response data are used as direct input to the equation of motion, from which the uncoupled mode shapes are obtained. The corresponding mass and stiffness matrices can be calculated using the condition of orthogonality of modes.

The phase II modeling utilized the same technique as described above, incorporating not only the lox

tank but also the thrust structure, outboard engine, and center engine crossbeam. The governing differential equation in generalized coordinates is

$$\{\ddot{q}_n\} + [2\zeta_n \omega_n] \{\dot{q}_n\} + [\omega_n^2] \{q_n\} = \left[\frac{1}{Mg_n} \right] [\phi]^T \{F \sin \omega t\}, \quad (1)$$

where

q_n = nth model coordinate

ω_n = natural frequency of nth mode

$\{\phi\}_n$ = nth modal column

$\{F \sin \omega t\}$ = applied force at frequency ω

ζ_n = damping of nth mode

Mg_n = generalized mass of nth mode.

The steady-state solution of equation (1) is

$$q_n = \frac{\left(\frac{\phi_{rn} F_{rn}}{Mg_n \omega_n^2} \right) \sin(\omega t + \psi_n)}{\left\{ \left(1 - \frac{\omega^2}{\omega_n^2} \right)^2 + \left(2\zeta_n \frac{\omega}{\omega_n} \right)^2 \right\}^{1/2}} \quad (2)$$

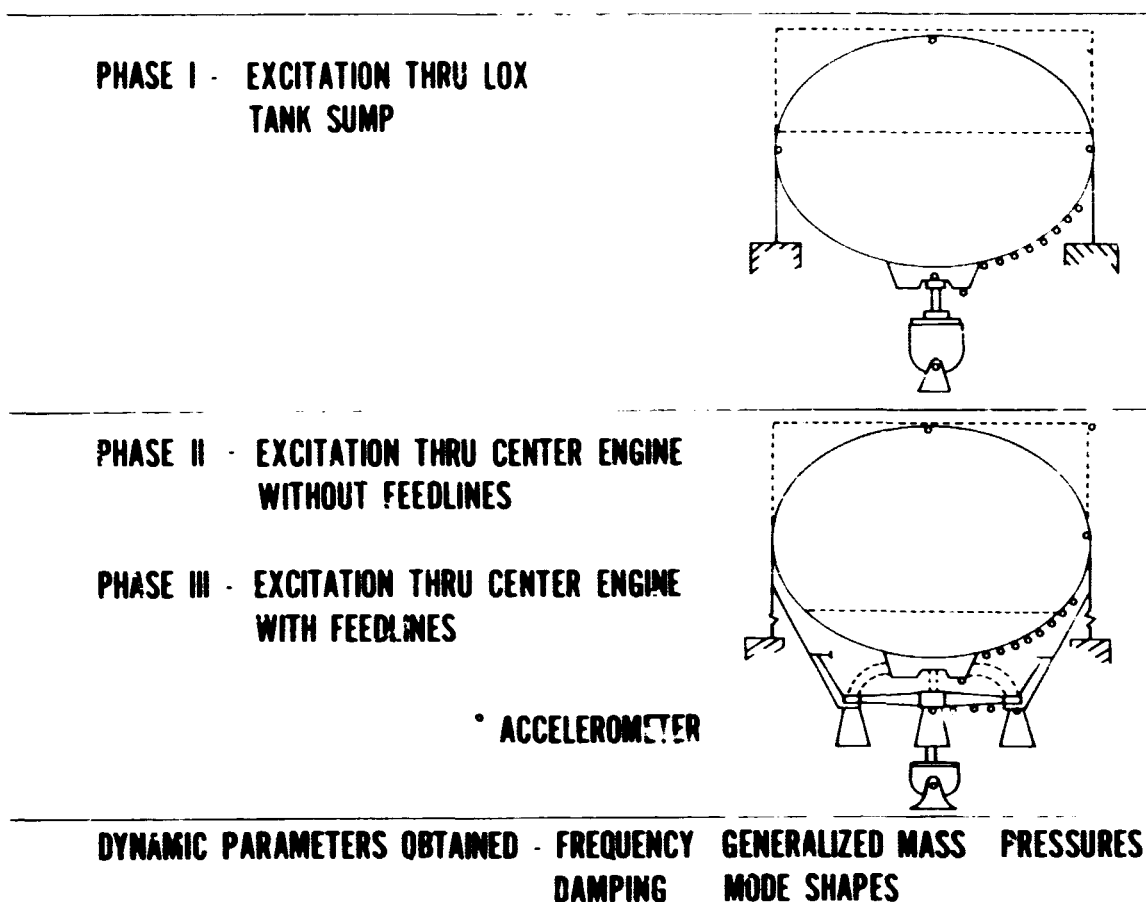


Figure 3. Test definition.

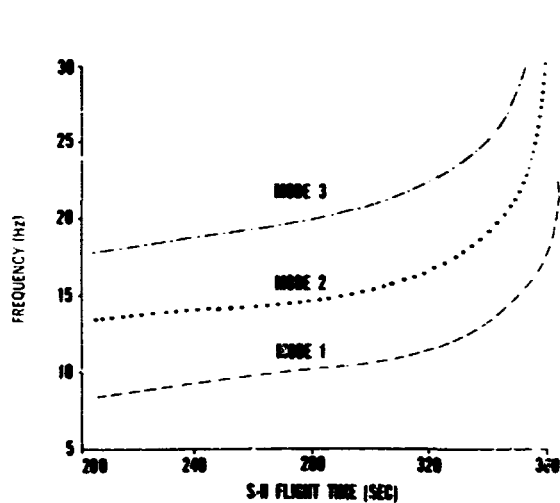


Figure 4. Phase I frequency versus time.

in which

$$\psi_n = \tan^{-1} \left[\frac{2\zeta_n \frac{\omega}{\omega_n}}{1 - \frac{\omega^2}{\omega_n^2}} \right]$$

and

$$q_n = \frac{X_{Sn}}{\phi_{Sn}}$$

where

 F_{rn} = applied force at point r in the n th mode ϕ_{rn} = modal displacement at point r in the n th mode ϕ_{Sn} = modal displacement at point S in the n th mode Y_{Sn} = real displacement at point S in the n th mode.

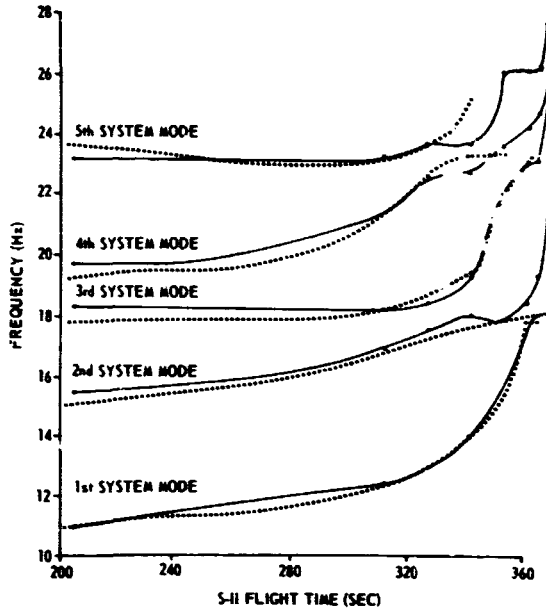


Figure 5. Phase II and III frequency versus time.

This substitution then results in the following equation:

$$\frac{X_{Sn}}{F_{rn}} = \frac{\left(\frac{\phi_{rn} \phi_{Sn}}{Mg_n \omega_n^2} \right) \sin(\omega t + \psi_n)}{\left\{ \left(1 - \frac{\omega^2}{\omega_n^2} \right)^2 + \left(2\zeta_n \frac{\omega}{\omega_n} \right)^2 \right\}^{1/2}} \quad (3)$$

If $\frac{X_{Sn}}{F_{rn}}$ is treated as forced response, one can

assume that it is comprised of the summation of the response contributions from each mode being analyzed. With this in mind, the following system of equations is obtained for response with an applied force at mode 1 with a forcing frequency of $\omega = \omega_1$:

$$\begin{aligned} C_{11}\phi_{11}^2 + C_{12}\phi_{12}^2 + \dots + C_{1n}\phi_{1n}^2 &= \frac{X_1}{F_1} \\ C_{11}\phi_{11}\phi_{21} + C_{12}\phi_{12}\phi_{22} + \dots + C_{1n}\phi_{1n}\phi_{2n} &= \frac{X_2}{F_2} \\ \vdots & \\ C_{11}\phi_{11}\phi_{n1} + C_{12}\phi_{12}\phi_{n2} + \dots + C_{1n}\phi_{1n}\phi_{nn} &= \frac{X_n}{F_n} \end{aligned}$$

The constants C_{ij} represent the coefficients of the modal displacement products $\phi_{rn} \phi_{sn}$ seen in

equation (3). The subscripts i and j refer to the forcing frequency ω_i and the modal resonant frequency ω_j , respectively. C_{ij} can be more specifically defined as follows:

$$C_{ij} = \frac{1}{\omega_j^2} \frac{\sin(\omega_i t + \psi_j)}{\left\{ \left(1 - \frac{\omega_i^2}{\omega_j^2} \right)^2 + \left(2\zeta_j \frac{\omega_i}{\omega_j} \right)^2 \right\}^{1/2}} \quad (4)$$

A similar set of equations may be obtained for every forcing frequency $\omega = \omega_i$ to $\omega = \omega_n$.

Careful examination of equation (4) reveals that the modal displacements are the only unknowns. All other parameters can be obtained for the test data. These unknowns $[\phi_{rn} \phi_{sn}]$ supply the information needed to define independent normal modes $[\phi]$ for the system.

Utilizing the conditions of orthogonality, the mass and stiffness matrices can be found in the following manner:

$$[M] = [\phi^T]_n^{-1} [Mg_n] [\phi]_n^{-1} \quad (5)$$

$$[K] = [\phi^T]_n^{-1} [Kg_n] [\phi]_n^{-1} \quad (6)$$

Several fill conditions were selected from each test phase. Modal frequencies, normal displacements, damping, and generalized mass from the dwell test data were input into equation (1), and normal modes were then substituted into equations (5) and (6).

COMPARISON OF TEST AND MODEL DATA

One check made on the developed model was a comparison of calculated response versus frequency with frequency response data obtained from the test. The model was derived using data obtained at resonant dwell points. As expected, exact agreement was shown at those points, as seen in Figure 6 and 7 for phase I and phase II comparisons, respectively. Also good agreement is shown at points other than resonance through the entire frequency range of interest. This indicates that the model adequately simulated the hydroelastic test system.

The total longitudinal mass of the system was determined from the generated mass matrices and is shown in Table 1 for the Phase II conditions. The total mass check was important, since this model

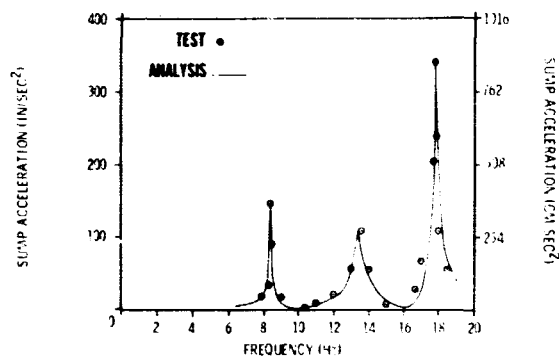


Figure 6. Phase I — model/test comparison (205-sec flight time).

would eventually be incorporated into a flight model of the Saturn V vehicle. No restraint had been placed on the magnitude of the mass matrix, but the table shows good agreement with actual test vehicle weights.

COMPARISON OF VEHICLE ANALYSIS AND FLIGHT DATA

It should be noted that the phase III test data were not used in deriving a final model for use in vehicle analysis. A comparison between the phase II and phase III data did not reveal an anomaly induced by the addition of engine feedlines. It was, therefore, concluded that the line definition that had been previously used would be incorporated and that phase II data adequately defined the thrust structure/

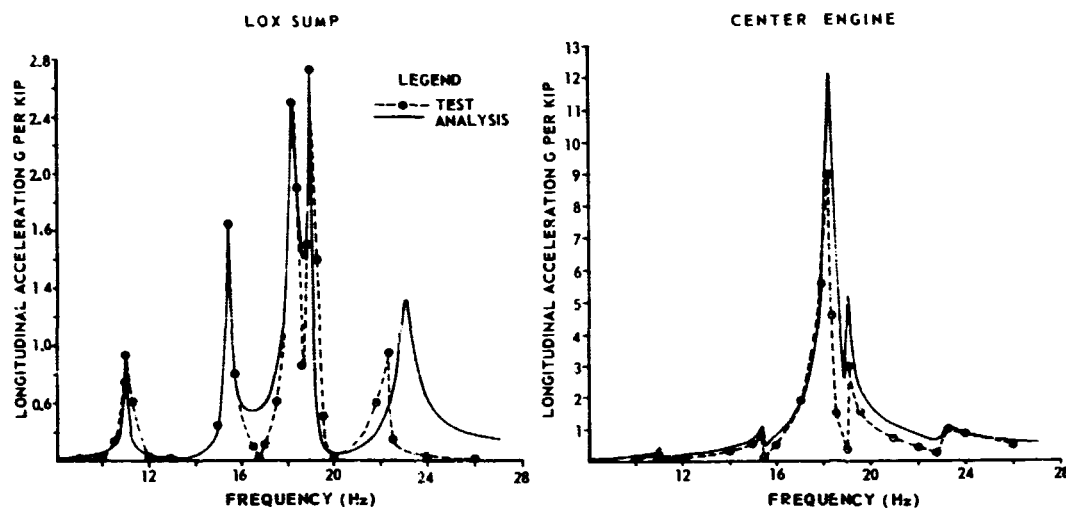


Figure 7. Phase II — model/test comparison (205-sec flight time).

TABLE 1. COMPARISON OF ACTUAL WEIGHTS WITH WEIGHTS CALCULATED FROM MASS MATRICES

| S-II Flight Time, sec | Actual Weight, kg (lb) | Mass Matrix Weight, kg (lb) | Percent Error |
|-----------------------|------------------------|-----------------------------|---------------|
| 205 | 207 445 (457 330) | 218 051 (480 711) | +5.11 |
| 313 | 97 447 (214 830) | 119 750 (264 000) | +22.8 |
| 328 | 84 001 (185 187) | 82 826 (182 597) | -1.39 |
| 341 | 72 489 (159 588) | 71 851 (156 977) | -2.26 |
| 352 | 62 882 (138 629) | 62 847 (138 332) | -0.02 |
| 361 | 55 772 (122 954) | 55 903 (123 243) | +0.02 |
| 364 | 52 853 (116 496) | 52 759 (116 311) | -0.01 |
| 370 | 50 197 (110 663) | 51 482 (113 496) | +2.56 |

center engine crossbeam/bulkhead system. A model derived from these data was then incorporated into the total Saturn V vehicle (Fig. 8), which contains spring-mass representations of the remaining flight structure. Figure 9 shows a comparison of a frequency analysis of the Saturn V S-II stage burn model versus AS-504, AS-507, and AS-508 flight data. The first three modes seen on the chart are major vehicle longitudinal modes. The next three modes represent the first and second predominant bulkhead modes and the predominant crossbeam mode, respectively. It is apparent that the flight data generally follow the predominant second bulkhead mode. However, no definite conclusion can be drawn from this analysis, since such parameters as forcing function, control systems, and engine transfer functions were not incorporated.

Approximate flight time for the POGO instability on AS-504 was at 340 seconds into the S-II stage burn.

The AS-507 flight did not experience this instability because of the center engine shutdown at about 60 seconds, before the end of S-II burn. This was done to open the unstable regenerative loop developed on flights such as AS-504. The AS-508 flight also had a scheduled early center engine shutdown; however, POGO developed at about 170 seconds into S-II burn, and an unscheduled center engine shutdown was effected because of excessive vibration levels.

CONCLUSIONS

It has been shown that the aft end of the S-II stage, including such complex components as bulkhead/fluid, thrust structure engines, and crossbeam, was successfully tested and mathematically

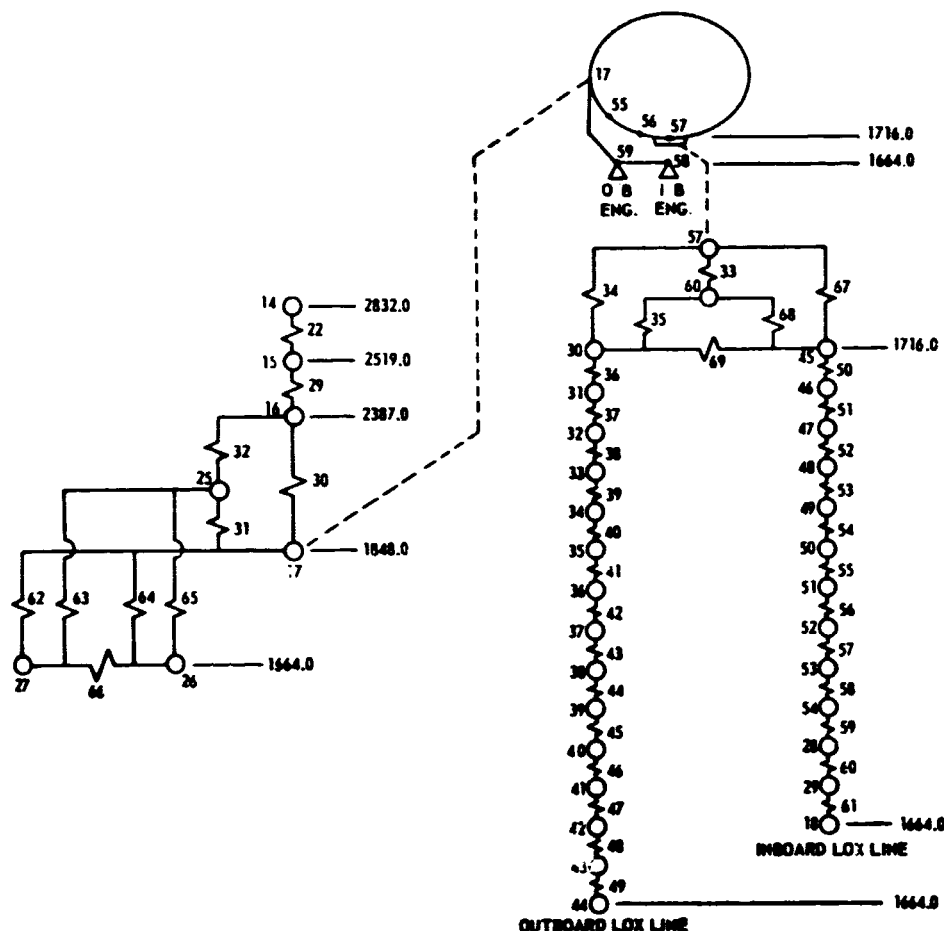


Figure 8. S-II flight model.

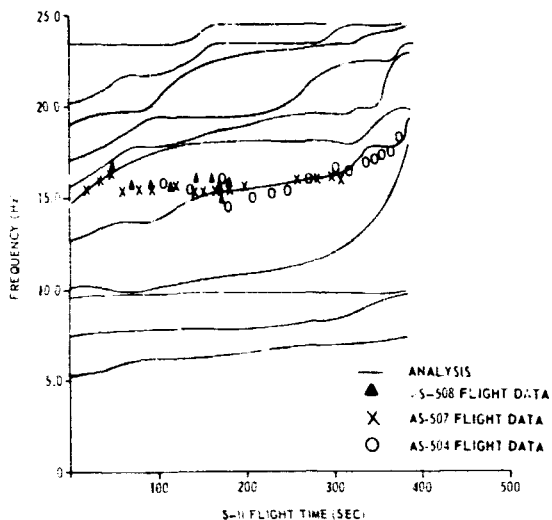


Figure 9. Flight data versus flight model.

REFERENCE

1. Thoren, A. R.: Preliminary Evaluation of S-II Mini-Test Results. Brown Engineering Technical Letter ASD-ASTNL-706, Huntsville, Alabama, 1969.

modeled. The results yielded an excellent frequency response and mass characteristics correlation. These models were incorporated into overall flight vehicle models and analyzed for modal parameters. Preliminary comparisons of frequency analysis with actual flight data indicate that the total structural modeling program has produced a good representation of the flight vehicle. Actual POGO instability analyses will be performed later utilizing these test-developed models along with other propulsion and control system transfer function modeling data. Future Saturn V flight vehicles will also be evaluated for this oscillatory problem when the model is able to reproduce all responses observed on previous vehicles.

APPROVAL

TM X-64528

RESEARCH ACHIEVEMENTS REVIEW
VOLUME IV REPORT NO. 1

The information in these reports has been reviewed for security classification. Review of any information concerning Department of Defense or Atomic Energy Commission programs has been made by the MSFC Security Classification Officer. These reports, in their entirety, have been determined to be unclassified.

These reports have also been reviewed and approved for technical accuracy.

Karl L. Heimburg
KARL L. HEIMBURG
Director, Astronautics Laboratory